Reducing Cofilin dosage makes embryos resilient to heat stress

Natalie Biel[1,2], Faizan Rashid[2, 10], Subhashis Natua[3, 10], Ting-Yu Wang[4], Tsui-Fen Chou[5],

Thu Vu Phuc Nguyen[6, 11], Ido Golding[6, 7], Auinash Kalsotra[3, 8, 9], Anna Marie Sokac[2, 12, *]

[1] Integrative Molecular and Biomedical Sciences Program,

Baylor College of Medicine, Houston, TX, 77030 USA

[2] Department of Cell and Developmental Biology,

University of Illinois Urbana-Champaign, Urbana, IL 61801, USA

[3] Department of Biochemistry,

University of Illinois Urbana-Champaign, Urbana, IL 61801, USA

[4] Division of Biology and Biological Engineering,

California Institute of Technology, Pasadena, CA 91125, USA

[5] Proteome Exploration Laboratory, Beckman Institute,

California Institute of Technology, Pasadena, CA 91125, USA

[6] Department of Physics,

University of Illinois Urbana-Champaign, Urbana, IL 61801, USA

[7] Department of Microbiology,

University of Illinois Urbana-Champaign, Urbana, IL 61801, USA

[8] Carl R. Woese Institute for Genomic Biology,

University of Illinois Urbana-Champaign, Urbana, IL 61801, USA

[9] Division of Nutritional Sciences,

University of Illinois Urbana-Champaign, Urbana, IL 61801, USA

[10] These authors contributed equally.

[11] Present address: Department of Molecular Biology,

Princeton University, Princeton, NJ 08544, USA

[12] Lead contact

*Correspondence: asokac@illinois.edu

Abstract

In addition to regulating the actin cytoskeleton, Cofilin also senses and responds to environmental stress. Cofilin can promote cell survival or death depending on context. Yet, many aspects of Cofilin's role in survival need clarification. Here, we show that exposing early *Drosophila* embryos to mild heat stress (32°C) induces a Cofilin-mediated Actin Stress Response and upregulation of heat- and ER- stress response genes. However, these responses do not alleviate the negative impacts of heat exposure. Instead, heat stressed embryos show downregulation of hundreds of developmental genes, including determinants of the embryonic body plan, and are less likely to hatch as larvae and adults. Remarkably, reducing Cofilin dosage blunts induction of all stress response pathways, mitigates downregulation of developmental genes, and completely rescues survival. Thus, Cofilin intersects with multiple stress response pathways, and modulates the transcriptomic response to heat stress. Strikingly, Cofilin knockdown emerges as a potent pro-survival manipulation for embryos.

Introduction

Cofilin is best known as a critical regulator of actin cytoskeleton organization and dynamics [1]. Cofilin binds actin filaments (F-actin) and drives their depolymerization or stabilization at low or high cofilin-to-actin ratios, respectively [2,3]. In this way, Cofilin tunes the polymerization cycle to control the assembly and disassembly of actin structures. Cofilin is itself regulated by upstream signaling that imparts instructions for how and when the actin cytoskeleton should be remodeled [4]. Conserved phosphatases, Slingshot and Chronophin, activate Cofilin by dephosphorylating its serine 3 residue. Conversely, kinases, including LIM kinase, inactivate Cofilin by phosphorylating the same residue. In some cases, active Cofilin is also oxidized or subjected to other post-translational modifications to further modulate its localization or activity [4-6]. Ultimately, these signals, acting through Cofilin, allow cells to carry out vital functions, such as maintaining or changing their shape and endocytosing, sorting and trafficking cargoes [7].

But Cofilin also plays less well-known roles in cells. For example, Cofilin is the major importer of actin monomers (globular, G-actin) into the nucleus. Cofilin itself has a nuclear localization signal, and active dephosphorylated Cofilin can bind free G-actin as well as actin filaments [8-12]. Thus, Cofilin can ferry G-actin into the nucleus, with the help of Importin-α9 [13,14]. Once inside, both Cofilin and actin influence gene expression through RNA Polymerase II [14,15].

Cofilin also plays a surprising part in inducible stress response and cell survival. Because Cofilin can be regulated by oxidation, it serves as a redox sensor [16]. While Cofilin oxidation is a normal mode of signaling in some contexts, it also occurs when the redox state of cells is perturbed by oxidative stress [6,17-19]. When the stress persists (*i.e.*, is

chronic), oxidized Cofilin moves to the mitochondria to promote swelling, downregulation of respiration and opening of permeability transition pores [6]. Subsequent release of Cytochrome C into the cytosol then leads cells to commit to death programs including apoptosis, necrosis and ferroptosis [5,6,20]. Thus, Cofilin can act as a potent initiator of mitochondrial-dependent cell death; and Cofilin's experimental or pathological downregulation can be protective against cell death [5,6,18,20-22].

In another stress scenario, Cofilin is the principal mediator of an Actin Stress Response (ASR) [23,24]. ASR is associated with several clinical conditions, including nemaline myopathy, ischemic brain and kidney injury, and neurodegenerative diseases such as Alzheimer's and Huntingtin's [25-31]. The ASR is induced by oxidative stress as well as heat, hypoxia, ATP depletion, Aβ oligomers, and by organismal aging [32-36]. In the initial steps of ASR, Cofilin is hyperactivated, leading to the assembly of aberrant F-actin rods that are coated by high levels of dephosphorylated, and sometimes oxidized, Cofilin [37-39]. These rods become so stable that monomers within them do not turnover [33,39,40]. Rods frequently form in the cytoplasm but can also assemble in the cell's nucleus [11,25,33,41-44]. If the stress is transient, rods can be protective because they prevent actin, an ATPase, from burning unnecessary energy as part of the actin polymerization cycle [40,45]. However, in the face of chronic stress, these rods are detrimental to cell function. In neurons, solid actin rods that form along axonal shafts can physically block transport between the cell body and synapse, promoting synapse degeneration [35,36,46-48]. Again, Cofilin's downregulation can inhibit rod assembly and be protective against cell dysfunction and death [23,27,49].

Thus, in playing its diverse roles, Cofilin has a complex relationship with cell health and survival. On the one hand, Cofilin activity is necessary for normal actin dynamics and cell function. What's more, Cofilin can promote helpful responses to cellular stress as in the case of protective actin rod assembly. However, it is also increasingly clear that cells in adult organisms sustain stress better when Cofilin levels or activity are reduced [18,21,27,50-54]. In related observations, Cofilin knockdown also promotes drug resistance by poorly characterized mechanisms [55-57]. So, while Cofilin is an essential protein, it also emerges as an obstacle to cellular resilience particularly under stress conditions. Cofilin's participation in mitochondrial death pathways and aberrant actin rod formation provide obvious means to influence cellular outcomes. But it is unclear whether these actions fully account for Cofilin's antagonism of cell survival. As Cofilin emerges as a candidate for therapeutic intervention in cancer, stroke, and neurodegenerative contexts [48-51,57-59], it is imperative that we define the extent to which it interfaces with cell physiology and stress response.

In our own preliminary work with *Drosophila* embryos, we similarly saw hints that Cofilin, while essential for development, also reduces the organism's ability to withstand environmental stress [33,60-63]. At that time, we described a maladaptive ASR that is mediated by Cofilin in fruit fly embryos reared under mild heat stress at 32°C [33]. These embryos showed prominent assembly of nuclear actin rods and diminished larval hatching rates. When we reduced Cofilin's genetic dosage to block the ASR, we found that heat stressed embryos were more likely to survive [33].

Here, we sought to better understand how Cofilin dosage modifies the survival of heat stressed embryos. We initiated our study with the hypothesis that Cofilin negatively

impacts embryo physiology upon heat stress due to its role in actin disruption and the ASR. However, as we paired survival data with quantitative analysis of these actin phenotypes for two distinct heat stress exposures, acute and chronic, we were forced to reevaluate our thinking. To then get an unbiased view, we used whole embryo RNA sequencing to determine the transcriptomes of wild-type and Cofilin knockdown embryos upon exposure to acute or chronic heat stress at 32°C. We found unexpected interactions between Cofilin and heat and ER stress response pathways. In addition, we found that reducing Cofilin dosage leads to an alternative pro-survival response in which the developmental perturbations that accompany heat stress in wild-type embryos are largely circumvented.

Results

The survival of wild-type embryos is negatively impacted by mild heat stress, even when exposure is limited to earliest development

We previously observed that wild-type embryos reared in the presence of a mild heat stress at 32°C show decreased survival to the larval stage, minor disruption of cytoplasmic F-actin structures, and assembly of nuclear actin rods indicating induction of ASR [33,64]. When we reduced the dosage of Cofilin, the main driver of actin disruption and ASR, embryo survival was improved [33]. Based on these results, we hypothesized that actin disruption and ASR compromise embryo survival.

To test our hypothesis here, we extended our stress conditions to include two distinct heat stresses: Specifically, embryos were reared with either transient "acute" or continuous "chronic" heat stress at 32°C (1.5- or 12-hour exposure, respectively; Figure 1A). The 32°C exposure is considered a mild heat stress because heat shock response in *Drosophila* has typically been studied at 37-42°C [65-68]. Rearing at 18°C or 22°C served as control non-stressed conditions. All temperatures were chosen according to field standards and our prior work [33,64,69].

To first probe survival after acute or chronic heat stress, we performed hatching assays for hundreds of embryos and followed them through their life stages, progressing from embryos to larvae to pupae to adults. Embryos exposed to either acute or chronic heat stress were hand-selected at cellularization, approximately 2.5 hours post-fertilization, and shifted to 22°C to continue development to the larval or adult stage (Figure 1A). Control non-stressed embryos were reared at 18°C until cellularization and then shifted to 22°C, alongside their heat stressed counterparts. We found that wild-type

embryos exposed to either acute or chronic heat stress prior to cellularization show significantly reduced hatching as both larvae and adult flies (Figures 1B, 1C and S1A). Reduced survival was most pronounced for chronic heat stress for both life stages (Figures 1B and 1C). For example, compare larval hatching rates of 83.8 ± 3.0 % or 52.8 ± 10.2 % for acute versus chronic stress, respectively (mean ± SE). These results are consistent with other reports that embryos exposed to temperatures ≥ 29°C, even for short times, show compromised viability [70-73]. Interestingly, even though the heat stress was limited to earliest development, there were long-term implications for organismal survival to adulthood.
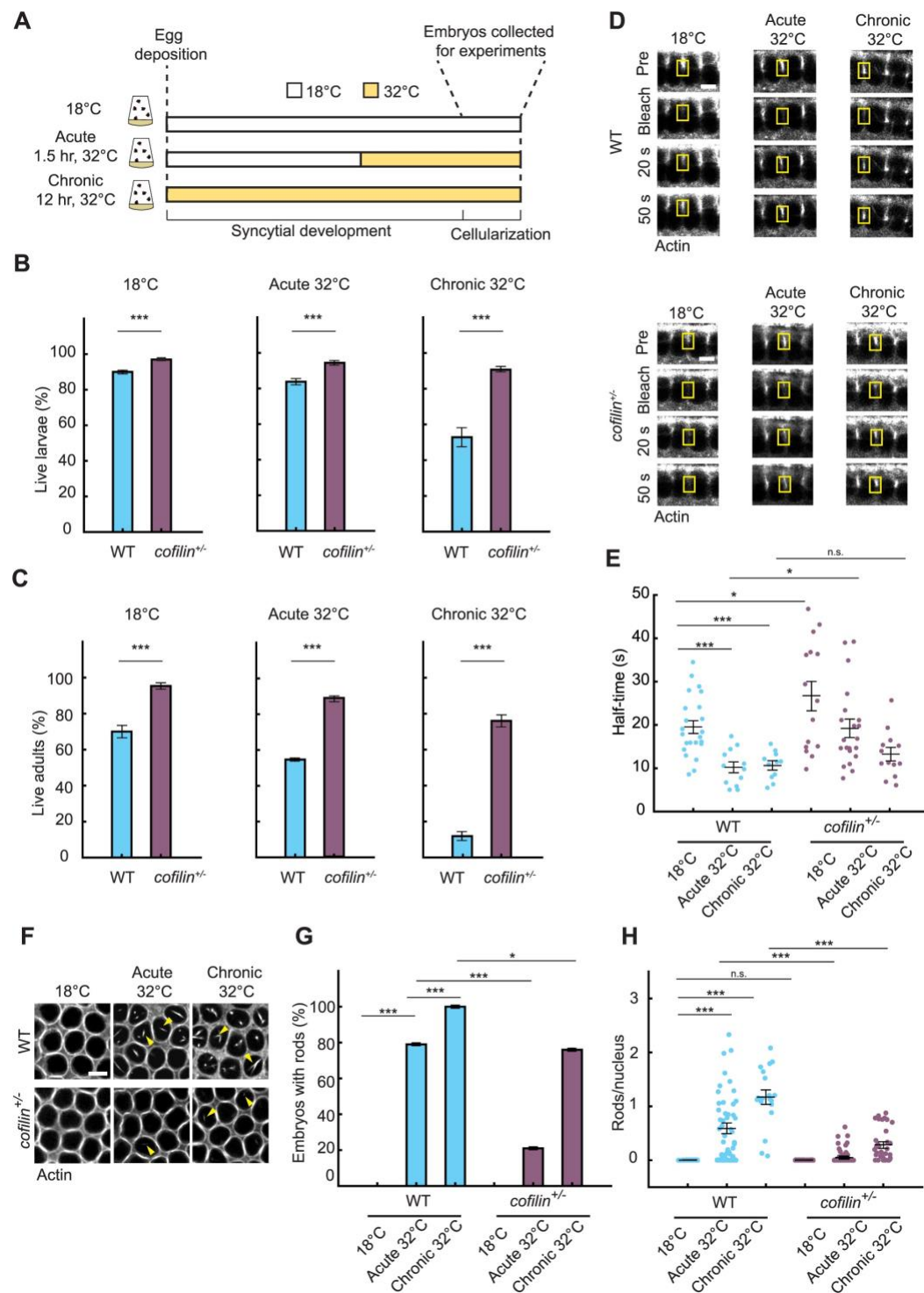
Figure 1. Cofilin knockdown rescues survival, but not by relieving actin disruption alone.

(A) Schematic showing heat stress exposure times relative to developmental

progression. Embryos collected at cellularization for experiments.

(B and C) Bar plots showing percentage of survival for larvae (B) and adult flies (C) for wild-type (WT; cyan) and *cofilin*$^{+/-}$ (purple) at indicated temperatures (n ≥ 600 embryos or n ≥ 150 embryos per condition for larval and adult survival assays, respectively).

(D) Cross-sections showing FRAP for furrow tip F-actin (G-actin^{Red}) in WT and *cofilin*$^{+/-}$ embryos at indicated temperatures. Frame "pre" collected immediately prior to bleaching; frames 20 seconds (s) and 50s collected after bleaching. Yellow box indicates bleached region. Scale bar: 5 μm.

(E) Dot plot showing half-time to recovery after photobleaching furrow tip F-actin for WT (cyan) and *cofilin*$^{+/-}$ (purple) embryos at indicated temperatures. Each point represents 1 embryo (n ≥ 11 embryos per condition, with 1 furrow bleached per embryo).

(F) Surface views showing G-actin^{Red} incorporated into furrow tips and nuclear actin rods (yellow arrowheads) in WT and *cofilin*$^{+/-}$ embryos at indicated temperatures. Scale bar: 5 μm.

(G) Bar plot showing percentage of WT (cyan) and *cofilin*$^{+/-}$ (purple) embryos with rods at indicated temperatures. (n ≥ 18 total embryos per condition, with ≥ 80 nuclei assayed per embryo).

(H) Dot plot showing rods per nucleus for WT (cyan) and *cofilin*$^{+/-}$ (purple) embryos at indicated temperatures. Each point represents 1 embryo (n ≥ 18 embryos per condition, with ≥ 80 nuclei counted per embryo).

The mean, shown as bars in (B), (C) and (G), or horizontal lines in (E) and (H), was calculated from n = 3 independent biological replicates. Error bars represent standard error of the mean (SE).

p-values for (B), (C) and (G) calculated using χ^2 contingency analysis.

p-values for (E) and (H) calculated using Student's t-test.

*** p < 0.0001, ** p < 0.001, * p < 0.05, p > 0.05 (not significant; n.s.)

Wild-type embryos exposed to heat stress show actin disruption, with severity that correlates with reduced survival

We next wanted to determine the extent of actin cytoskeleton disruption in wild-type embryos exposed to either acute or chronic heat stress. To assay the integrity of the cytoplasmic actin cytoskeleton, we focused on cellularization, the first tissue-building event in the embryo [74]. Successful cellularization critically depends on stable F-actin structures forming at the tips of invaginating cleavage furrows and normally results in the generation of an epithelial sheet of hexagonally arrayed mononucleate cells [74]. When F-actin tip structures are destabilized, some furrows regress, leaving multinucleate cells within the plane of the epithelial sheet [64,75-77]. We assayed for multinucleation, using a furrow marker, the Septin Peanut (*D.m.* Pnt). Wild-type embryos were fixed immediately after exposure to either acute or chronic heat stress at 32°C (Figure 1A). Control non-stressed embryos were reared at 18°C. The frequency of multinucleation increased in wild-type heat-stressed embryos (Figures S1B and S1C) and corresponded to an increase in the mean ratio of multinucleate cells to total nuclei per embryo (Figure S1D).

To ask whether furrow regression and multinucleation were accompanied by reduced F-actin stability at furrow tips, we used fluorescence recovery after photobleaching (FRAP) in live heat-stressed embryos [33,78,79]. FRAP measures the rate of actin monomer turnover in filaments, where faster turnover means filaments are less stable [80]. To visualize furrow tip F-actin, we injected heat- or non-stressed embryos with rhodamine-conjugated non-muscle G-actin (G-actin[Red]) at 30 minutes post egg deposition. G-actin[Red] incorporates into F-actin structures and preserves normal F-actin function in developing embryos [33,78,79]. Heat-stressed embryos were imaged on a

temperature-controlled stage at 32°C, while non-stressed embryos were imaged at 18°C. We found that the half-time to recovery was significantly faster for furrow tip structures upon either acute or chronic heat stress (Figures 1D and 1E). Thus, cytoplasmic F-actin structures are destabilized in wild-type embryos challenged by mild heat stress of both durations.

To next test for disruption of the nuclear actin cytoskeleton, we looked for assembly of aberrant nuclear actin rods in heat-stressed embryos. These rods are composed of parallel bundles of highly twisted F-actin and indicate induction of the ASR [37-39]. To visualize rods, we injected heat- or non-stressed wild-type embryos with G-actin^{Red}, followed by live imaging at 32°C or 18°C, respectively [33,81]. We collected single plane images that bisect nuclei. At this plane, F-actin is visible in furrow structures that encircle the dark nuclei (Figure 1F). In addition, nuclear actin rods were prominent in wild-type embryos exposed to either acute or chronic heat stress but were completely absent in non-stressed embryos at 18°C (Figure 1F). The fraction of wild-type embryos with rods and number of rods per nucleus were most elevated in the chronic heat stress condition (Figures 1G and 1H). In addition, actin rods had a larger diameter in wild-type embryos exposed to chronic versus acute stress (Figure S1E). Nuclear actin rods in both heat stress conditions were "stable" as determined by a lack of recovery of G-actin^{Red} signal within rods following FRAP (Figures S1F and S1G). These results show that stable nuclear actin rod formation increases with increasing severity of heat stress.

Thus, by extending our stress conditions here, we see that both the cytoplasmic and nuclear actin cytoskeleton are disrupted by acute and chronic heat stress in wild-type embryos. We found correlations between the severity of actin disruption and poor embryo

survival, particularly for rod assembly (R = -0.7 ± 0.3 and R = -0.93 ± 0.04 for multinucleation and rod assembly, respectively; Figures S1H and S1I). So far, our data is consistent with the hypothesis that heat-induced actin disruption leads to poor embryo survival.

The reduced survival of heat-stressed embryos is completely rescued by Cofilin knockdown

To further test our hypothesis that actin disruption leads to reduced embryo survival, we employed Cofilin. Cofilin is the main driver of the ASR [23,24], and we previously moderated cytoplasmic actin disruption and actin rod assembly in embryos by reducing the maternal dose of the *cofilin* gene (*i.e.* embryos were harvested from mothers heterozygous for a loss-of-function allele of *cofilin*) [33]. To determine how Cofilin knockdown influences embryo survival following the acute or chronic heat stress exposures here, we assayed hatching rates for *cofilin*$^{+/-}$ embryos (Figure 1A). We validated that knockdown reduces the Cofilin protein level to 62.5 ± 12.4 % of the wild-type level (mean ± SE; Figure S1J). Remarkably, *cofilin*$^{+/-}$ embryos showed significantly better survival than their wild-type counterparts at all conditions and at both larval and adult stages (Figures 1B, 1C and S1A). Even when comparing survival rates with no heat stress at 18°C, the *cofilin*$^{+/-}$ embryos have a survival advantage over wild-type embryos (Figures 1B and 1C). These results show that reducing the dosage of Cofilin makes embryos more resilient and fully suppresses the effects of heat stress on embryo survival, perhaps by counteracting negative impacts on the actin cytoskeleton.

Actin disruption accompanies reduced survival, but is not its sole determinant

We next examined the ability of Cofilin knockdown to curb actin disruption after each heat stress exposure (Figure 1A). For the cytoplasmic actin cytoskeleton, we saw no multinucleation in *cofilin*^{+/-} embryos following either acute or chronic heat stress at 32°C (Figures S1B, S1C, and S1D). Accordingly, the mean ratio of multinucleate cells to total nuclei equaled zero in heat-stressed *cofilin*^{+/-} embryos (Figure S1D). We also assayed the stability of furrow tip F-actin using FRAP. Non-stressed *cofilin*^{+/-} embryos at 18°C showed a slower half-time to recovery compared to non-stressed wild-type embryos (Figures 1D and 1E). Slower recovery indicates increased F-actin stability, which is predicted when Cofilin's F-actin depolymerization activity is decreased by reduced Cofilin dosage. Similarly, after acute heat stress, *cofilin*^{+/-} embryos showed slower recovery than their wild-type counterparts (compare 18.8 ± 2.0 and 10.2 ± 1.2 seconds, respectively; mean ± SE; Figure 1E), suggesting cytoplasmic F-actin destabilization was rescued in *cofilin*^{+/-} embryos at this condition. Unexpectedly, though, *cofilin*^{+/-} embryos exposed to chronic heat stress showed the same extent of destabilization as wild-type embryos under the same condition (compare 13.4 ± 1.5 seconds and 10.9 ± 1.0 seconds, respectively; mean ± SE; Figure 1E). Thus, Cofilin knockdown reduces but does not entirely counter disruption of the cytoplasmic actin cytoskeleton in heat-stressed embryos, particularly in the context of chronic heat stress.

To then test for assembly of nuclear actin rods and induction of ASR in *cofilin*^{+/-} embryos, we used the same G-actin[Red] injection and imaging method as described above. In 18°C non-stressed *cofilin*^{+/-} embryos, rods were absent inside nuclei, whereas nuclear rods were seen in *cofilin*^{+/-} embryos exposed to acute or chronic heat stress (Figures 1E

and 1F). However, we found that the fraction of *cofilin*$^{+/-}$ embryos with rods and number of rods per nucleus were significantly decreased compared to wild-type embryos, for both stress conditions (Figures 1G and 1H). Nuclear actin rods were also thinner in *cofilin*$^{+/-}$ embryos for both stress conditions (Figure S1E). These rods were, nonetheless, stable as determined by photobleaching (Figures S1F and S1G), suggesting that a lack of turnover of actin monomers is a general feature of rods in embryos, regardless of stress condition or genotype.

Overall, actin disruption and the ASR were reduced following knockdown of Cofilin. However, our results for *cofilin*$^{+/-}$ embryos also argue that the disruption of cytoplasmic F-actin and/or presence of stable nuclear rods is not a simple one-to-one predictor of embryo survival. Regarding cytoplasmic F-actin, *cofilin*$^{+/-}$ embryos exposed to chronic heat stress showed the same extent of destabilization as wild-type embryos but had a much higher survival rate (Figures 1B, 1C and 1E). Also, in the chronic stress condition, 76.14 ± 0.05 % of *cofilin*$^{+/-}$ embryos assembled nuclear actin rods (mean $\pm$ SE), but these embryos had the same survival rate as non-stressed wild-type embryos that assembled no rods (Figures 1B, 1C and 1G). While we find that the severity of actin disruption correlates with decreased survival (Figures S1H and S1I), our data fails to support the hypothesis that these disruptions are the sole driver of poor survival in wild-type embryos. Instead, we suggest that unknown factors in addition to actin disruption and ASR compromise survival in heat stressed wild-type embryos, and Cofilin knockdown somehow counters these factors to make embryos resilient to the stress.

In wild-type embryos, heat stress upregulates heat and ER stress response genes and downregulates developmental genes

The actin cytoskeleton is unlikely to be the only subcellular system disrupted by heat stress, and other responses may be more closely linked to decreased survival [82]. To gain a more comprehensive readout of the changes taking place in heat-stressed embryos, we performed whole-embryo RNA sequencing (RNA-Seq). We considered that whole-embryo sequencing was preferable at this early stage of development because cell-type specification is only starting at this time. Wild-type embryos were exposed to acute or chronic stress at 32°C as in the earlier experiments (Figure 1A), and poly-A RNA was extracted at Bownes Stage 5, corresponding to early/mid cellularization [83]. Six independent biological replicates were run per condition. Following sequencing, we identified significantly up- or down- regulated genes (p < 0.05) in heat-stressed wild-type embryos versus their non-stressed siblings at 18°C. Because the maternal-to-zygotic transition (MZT) is ongoing at Stage 5, detected genes can represent both maternally and zygotically contributed transcripts [84]. To validate RNA-Seq results, we compared with expression profiles determined by quantitative PCR (qPCR). The same trends of differential expression were observed by both methods for 13 out of 14 cases (>92% reproducibility; Figure S2A; Table S1). Finally, we performed gene enrichment analysis on each set of up- or down- regulated genes per condition using PANGEA to identify the most statistically significant ontologies (p < 0.02) [85].

For wild-type embryos exposed to acute stress, 661 genes were significantly upregulated and 380 downregulated (Figure 2A; Table S2). Among the upregulated genes, a response to heat stress was evident by increased expression of chaperones

and heat shock proteins (Hsps; Figures 2A, 3C and S2B). To test whether transcripts encoding Hsps were translated, we cut bands from SDS-PAGE gels at molecular weights of 20-30 and 60-80 kilodaltons and determined the proteins present by mass spectrometry. In two independent experiments, we detected the induction of Hsp70Aa/Ab, as well as Hsp22, the latter of which was absent from the RNA-Seq data (Figure S3A; Table S2 and S3). The expression of Hsps 23, 26, 27, 60A, 68, 83, and Hsc70Cb/Hsp110 was also detected in both mass spectrometry experiments. Other significant ontologies identified from the RNA-Seq analysis were consistent with induction of heat stress response, including protein refolding (Figure S2B; Table S4). Among the downregulated genes there was enrichment for functions related to development, with ontologies including words such as "fate determination" and "morphogenesis" (Figure S2B; Table S4), suggesting mild perturbation of developmental processes.

More genes were differentially expressed in wild-type embryos exposed to chronic heat stress, with 1361 significantly upregulated and 1116 downregulated (Figure 2B; Table S2). But while the total number of differentially expressed genes was more than double in the chronic versus acute stress condition, there was overlap between the significant ontologies (Figures S2B and S2C; Table S4). Again, heat stress response indicators were upregulated, while developmental genes were downregulated (Figures 2B and S2C). We noted that the fold change (FC) among upregulated Hsps was frequently lower in the chronic than acute condition (Figure 3C), perhaps because these embryos are exhibiting adaptation to heat as a prolonged stressor rather than a transient assault (for example, compare $\log_2(FC)$ = 2.4 or 4.5 for Hsp68 after chronic or acute stress, respectively, and Hsp70Ab was absent in the chronic stress condition; Figure 3C).

Unique to chronic heat stress, the ontology for endoplasmic reticulum (ER) unfolded protein response appeared for the upregulated genes (Figures S2B and S2C; Table S4). Genes related to ER stress response included Calreticulin (Calr), Calnexin 99A (Cnx99A), Edem2, septin interacting protein 3 (sip3), Xbp1 and Ire1 (Figures 2B and 3D). Induction of ER stress response is known to be particularly harmful to early mammalian embryos, consistent with our observation that chronic heat stress leads to reduced survival in fly embryos (Figures 1B and 1C) [86,87].

Considering the downregulated genes, the developmental program was perturbed to a striking extent in the chronic heat stress condition. Normally at stage 5, embryos are undergoing extensive transcriptional remodeling during the MZT, splicing patterns are changing, chromatin is reorganized, the body plan is being established, and morphogenesis is starting [84,88-91]. All these processes are represented by the ontologies of the downregulated genes in embryos exposed to chronic heat stress (Figure S2C). We focused on the blastoderm segmentation genes because they represent a well-defined module, necessary for successful embryogenesis, and their transcriptional patterns have been comprehensively documented [92,93]. Considering the "gap" and "pair-rule" genes within the anterior-posterior (AP) determination pathway, we found that 15 genes out of a core set of 24, as defined by the Interactive Fly database (Table S4), are perturbed (2 upregulated, 13 downregulated; Figures 2B and 3E). The "segment polarity" genes, engrailed and invected (en and inv, respectively), which are also critical to AP determination, do not appear in our data set because their zygotic transcription is normally turned on just after the time when we collected embryos for our experiments [94].

Dorsal-ventral (DV) patterning also appeared as a significant ontology for the downregulated genes in wild-type embryos after chronic heat stress (1 upregulated and 7 downregulated; Figure S2C). We used RNA fluorescence *in situ* hybridization (RNA FISH) to validate the downregulation of *twist* (*twi*), a critical gene in DV patterning whose precise transcription during Stage 5 is necessary for ventral furrow formation immediately following cellularization [95,96]. As expected, within the band of cells that will invaginate to become the ventral furrow, RNA FISH for *twist* showed both diffuse mRNA in the cytoplasm and nascent transcriptional foci at the two gene copies in nuclei (Figure 2C) [95]. In embryos exposed to chronic heat stress at 32°C, the width of the ventral tissue band, as defined by *twist* expression being "on", was ~8 cells smaller than in non-stressed control embryos reared at 18°C (Figures 2C and 2D). Moreover, the number of nuclei showing transcription from both copies of the gene was significantly reduced (Figure 2E). According to previous reports, this degree of perturbation to *twist* expression, or that of *snail* (*sna*), another DV gene that also appeared among the downregulated genes in chronically heat-stressed wild-type embryos (Table S2), is sufficient to disrupt ventral furrow formation [95,97].

Combined, our data for wild-type embryos shows that even mild heat stress at 32°C is sufficient to upregulate heat and ER stress response genes, in addition to inducing the ASR (Figures 1 and S1). To the best of our knowledge, this is the first study to report signs of ER stress response in heat-stressed fly embryos. These stress responses, however, offer limited protection against elevated temperature, as judged by reduced embryo survival (Figures 1B and 1C). Furthermore, these responses fail to buffer a simultaneous large-scale perturbation of the gene expression program required for

normal development (Figures 2, 3E, S2B and S2C). We found that the number of perturbed gap and pair-rule genes, as well as the sum of their $\log_2$(FC), is highly correlated with reduced survival (R = 0.87 ± 0.02 and R = 0.97 ± 0.01, respectively; Figures S2F, S2G and S2H); and there appears to be a catastrophic collapse of survival as the number of perturbed segmentation genes increases (Figure S2H). In addition to embryo AP and DV patterning pathways, ontologies relevant to other aspects of embryogenesis and morphogenesis are also enriched among downregulated genes (Figures S2B and S2C; Table S4), revealing a multitude of threats to development in heat stressed wild-type embryos.
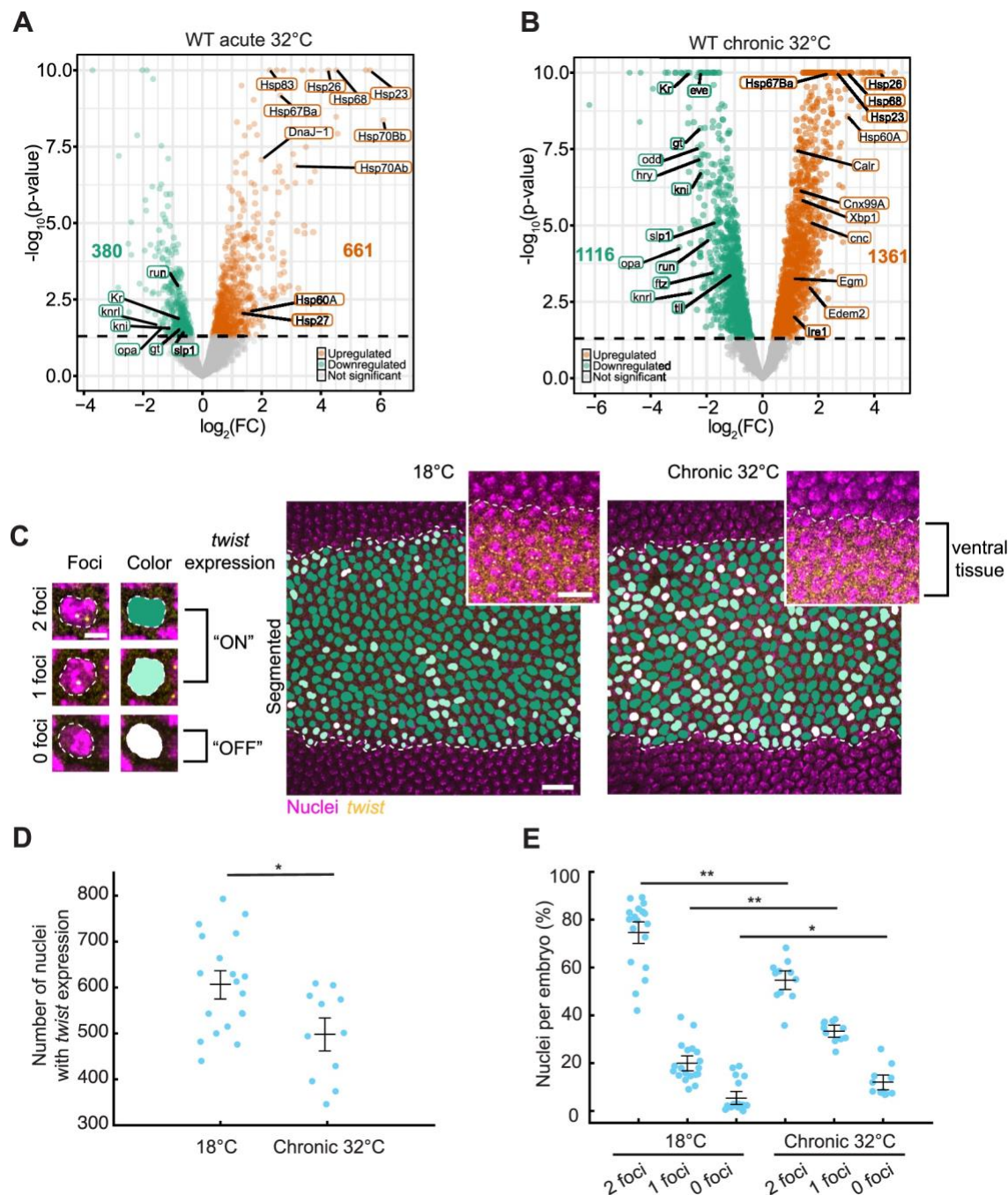
Figure 2. Heat stressed wild-type embryos show upregulation of heat and ER stress

response genes and downregulation of developmental genes.

(A and B) Volcano plots showing $\log_2$(FC) versus -$\log_{10}$(p-value) for upregulated

(orange) and downregulated (green) genes in acute 32°C (A) or chronic 32°C (B) heat

stressed wild-type (WT) embryos relative to 18° non-stressed WT embryos. Number of up- or down-regulated genes shown in bold.

(C) Segmented maximum intensity projections (MIPs; right) showing expression of *twist* by RNA-FISH in WT embryos at indicated temperatures. Outlined regions indicate the ventral tissue band where *twist* mRNA (gold) is seen as distinct foci in the nuclei and diffuse signal in cytoplasm (inset, bracketed region). At left, individual nuclei (outlined) with 0, 1, or 2 transcriptional foci are color-coded as in the segmented MIPs. For nuclei with 1 or 2 foci, *twist* expression is considered "on". Scale bars: 2 µm for individual nuclei; 10 µm for insets; 50 µm for segmented MIPs.

(D) Dot plot showing number of nuclei with *twist* expression (1 or 2 foci) per WT embryo at indicated temperatures ($n \geq 12$ embryos per condition).

(E) Dot plot showing percentage of nuclei with corresponding number of *twist* transcriptional foci per WT embryo at the indicated temperatures ($n \geq 12$ embryos per condition).

Differential gene expression data in (A) and (B) based on $n = 5$ biological replicates for chronic 32°C heat stressed WT embryos or $n = 6$ for all other conditions. Significance value cut-off for genes was $p < 0.05$.

The mean, shown as horizontal lines in (D) and (E), was calculated from $n = 3$ independent biological replicates. Error bars represent standard error of the mean (SE).

*** $p < 0.0001$, ** $p < 0.001$, * $p < 0.05$, $p > 0.05$ (not significant; n.s.).

In Cofilin knockdown embryos, the transcriptional response to heat stress is blunted

Given that Cofilin knockdown leads to significantly improved survival compared to the wild-type genotype (Figures 1B and 1C), we wanted to also determine how *cofilin*^{+/-} embryos respond to heat stress. We repeated RNA-Seq as described above, performing six independent biological replicates per stress condition for *cofilin*^{+/-} embryos. Two replicates of wild-type embryos were also included per condition so that experimental results between genotypes and experiments could be made with minimal concern regarding batch effects. Significantly up- or down- regulated genes (p < 0.05) were determined by comparing heat-stressed *cofilin*^{+/-} embryos to their non-stressed siblings reared at 18°C. Enrichment analysis was performed on each of the differentially expressed gene sets per condition, using PANGEA to identify the most highly significant ontologies (p ≤ 0.02) [85].

After acute heat stress at 32°C, 436 genes were significantly upregulated and 305 downregulated in *cofilin*^{+/-} embryos (Figure 3A; Table S2). This was a more muted response than seen in the acute stress condition for wild-type embryos (compare a total 741 differentially expressed genes in *cofilin*^{+/-} versus 1041 genes in wild-type; Figures 2A and 3A). As in wild-type, some Hsp genes were upregulated in *cofilin*^{+/-} embryos (Figures 3A and 3C; Table S2) and mass spectrometry showed reproducible induction of Hsp68 and Hsp70Aa/Hsp70Ab protein in *cofilin*^{+/-} embryos (Figure S2B; Table S3). However, compared to wild-type, fewer Hsp genes were upregulated, their fold-change was less (with Hsc-4 as the only exception), and no "heat" specific ontology was present among the significant ontologies for *cofilin*^{+/-} embryos (Figures 3C and S2D; Table S4). Other

ontologies for the upregulated genes were consistent with induction of stress response in *cofilin*$^{+/-}$ embryos after acute heat stress, including "chaperone mediated protein folding" and "oxidation-reduction process" (Figure S2D; Table S4). But, again, fewer genes were affected in *cofilin*$^{+/-}$ versus wild-type embryos. For example, for oxidation-reduction process, 15 genes were upregulated in *cofilin*$^{+/-}$ embryos (with sum of $\log_2(FC) = 22.9$), while 22 genes were upregulated in wild-type embryos (with sum of $\log_2(FC) = 27.5$). No ontology for ER stress response genes was identified. Combined, these results suggest that *cofilin*$^{+/-}$ embryos detect acute heat stress at 32°C, but they induce expression of fewer stress response genes compared to their wild-type counterparts.

This attenuated response was similarly reflected by the downregulated genes. For *cofilin*$^{+/-}$ embryos exposed to acute heat stress, ontologies related to development were present, as seen for wild-type embryos (Figure S2D; Table S4). However, taking the core set of segmentation genes as an example, no gap or pair-rule genes were significantly downregulated in *cofilin*$^{+/-}$ embryos compared to 7 out of 24 downregulated genes in wild-type embryos (Figure 3E). For DV patterning, neither *twist* nor *snail* were differentially expressed in *cofilin*$^{+/-}$ embryos. Taking a broader view of development, we manually curated a list of 95 genes based on searches for ontology terms including the words "embryo", "embryonic" and "embryogenesis" (Table S4). Whereas 15 genes changed in *cofilin*$^{+/-}$ embryos (7 upregulated and 8 downregulated, with sum of $\log_2(FC) = 0.5$), 29 genes were differentially expressed in wild-type embryos (8 upregulated and 21 downregulated, with sum of $\log_2(FC) = -6.8$). Similarly, we curated a list of 391 genes based on ontology terms including the word "morphogenesis" (Table S4) and found 63 genes changed in *cofilin*$^{+/-}$ embryos (24 upregulated and 39 downregulated, with sum of

$\log_2(FC) = 2.6$) compared to 101 genes that were differentially expressed in wild-type (27 upregulated and 74 downregulated, with sum of $\log_2(FC) = -35.7$). Thus, the reduction of Cofilin dosage somehow buffered the perturbation to developmental gene expression caused by acute heat stress.

Even when challenged by chronic heat stress, *cofilin*$^{+/-}$ embryos showed an attenuated response, where 756 genes were significantly upregulated and 632 downregulated (compare a total 1388 differentially expressed genes in *cofilin*$^{+/-}$ versus 2477 genes in wild-type; Figures 2B and 3B; Table S2). Response to heat was seen among the ontologies for the up-regulated genes in *cofilin*$^{+/-}$ embryos (Figure S2E; Table S4). But again, fewer genes changed (9 versus 13) and the change was to a lesser extent in *cofilin*$^{+/-}$ versus wild-type embryos (Figure 3C). In contrast to wild-type embryos, ER stress response was not identified as a significant ontology among upregulated genes in chronically stressed *cofilin*$^{+/-}$ embryos (Figures 3D and S2E; Table S4). Also, in contrast to wild-type embryos, developmental genes and processes did not appear among the significant ontologies for the downregulated genes in *cofilin*$^{+/-}$ embryos (Figure S2E; Table S4). Looking specifically at the core gap and pair-rule genes in the chronic heat stress condition, there were only 4 downregulated genes in *cofilin*$^{+/-}$ embryos compared to 13 in wild-type embryos and the extent of reduction was less (Figure 3E). The DV genes, *twist* and *snail* were not differentially expressed in *cofilin*$^{+/-}$ embryos.

Considering the "embryo", "embryonic" and "embryogenesis" related ontologies for chronic heat stress (Table S4), whereas 26 genes changed in *cofilin*$^{+/-}$ embryos (13 upregulated and 13 downregulated, with sum of $\log_2(FC) = 5.5$), 72 genes were differentially expressed in wild-type embryos (25 upregulated and 47 downregulated, with

sum of $\log_2$(FC) = -28.1). Similarly, for the "morphogenesis" related ontologies (Table S4), we found 122 genes changed in *cofilin*$^{+/-}$ embryos (55 upregulated and 67 downregulated, with sum of $\log_2$(FC) = 13.5) compared to 258 genes that were differentially expressed in wild-type (99 upregulated and 159 downregulated, with sum of $\log_2$(FC) = -70.3). So again, reduced Cofilin dosage muted the perturbation to developmental gene expression caused by chronic heat stress.

Overall, *cofilin*$^{+/-}$ embryos exposed to either acute or chronic heat stress showed, not only a blunted, but also a distinct transcriptional response compared to wild-type. For example, in addition to the differences noted above for heat and ER stress response genes and developmental genes, the most significant ontology identified for upregulated genes in *cofilin*$^{+/-}$ embryos, after both acute and chronic heat stress, was transmembrane transport (Figures S2D and S2E; Table S4). Yet, this ontology did not appear as highly significant for wild-type embryos under either heat stress condition (Figures S2B and S2C; Table S4). In total, only 201 differentially expressed genes were shared between *cofilin*$^{+/-}$ and wild-type embryos exposed to acute stress (total intersection = 133 upregulated genes + 68 downregulated genes; Figure 4A); and 500 genes were shared between *cofilin*$^{+/-}$ and wild-type embryos exposed to chronic stress (total intersection = 303 upregulated genes + 197 downregulated genes; Figure 4B). Thus, the majority of differentially expressed genes are exclusive to only the *cofilin*$^{+/-}$ or wild-type embryos for both stress conditions. Our data suggests that knocking down Cofilin levels largely alleviates the impacts of stress that were seen on the wild-type transcriptome. Instead, *cofilin*$^{+/-}$ embryos pursue an alternative response when challenged by heat stress. Taking all our data into account, we suggest that Cofilin knockdown does not rescue embryo

survival solely by countering actin disruption and ASR, as we initially hypothesized. Rather, Cofilin knockdown leads to a unique wide-ranging transcriptomic response that supports embryo survival.
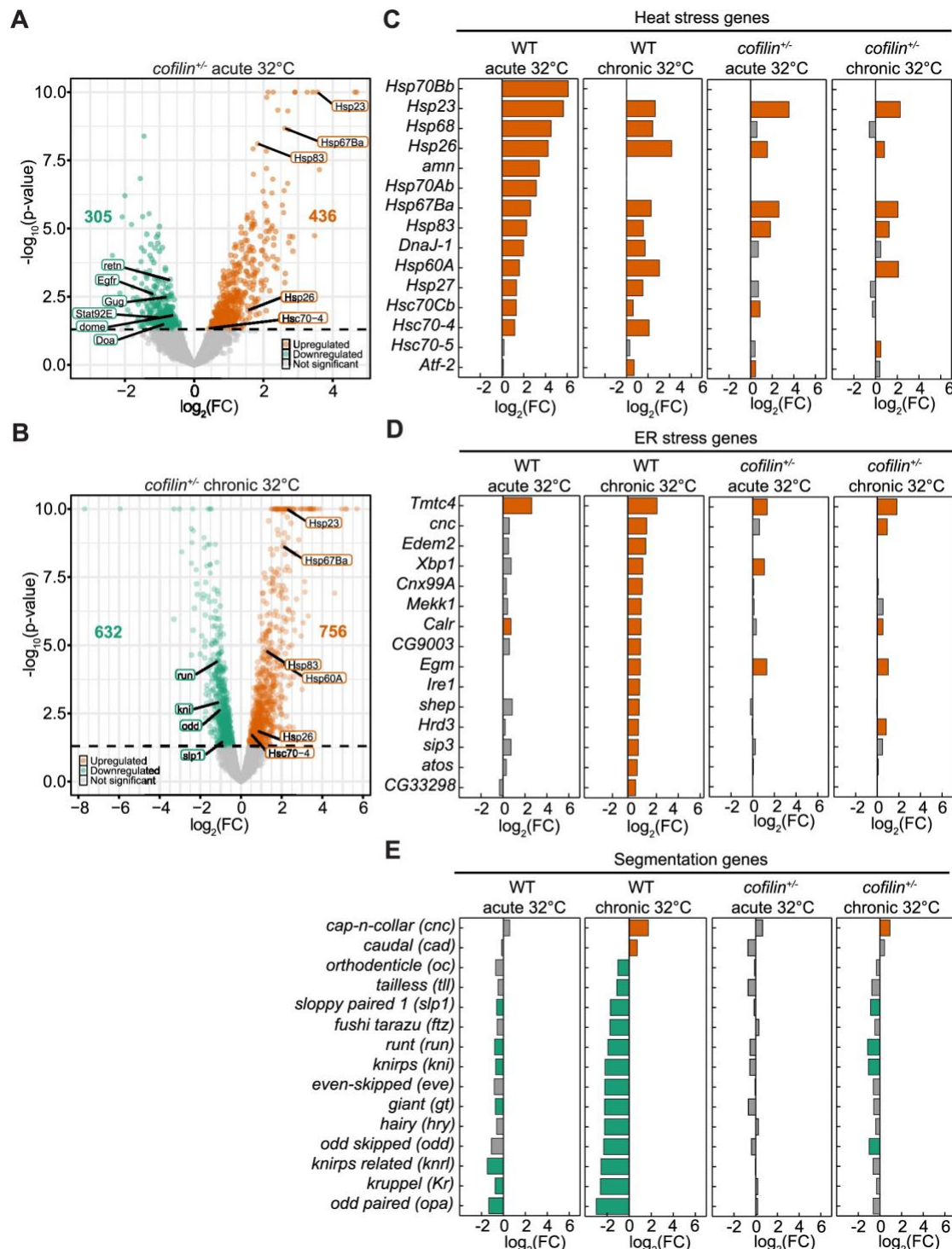
Figure 3. In *cofilin+/-* embryos the transcriptional response to heat stress is blunted.

(A and B) Volcano plots showing $\log_2$(FC) versus $-\log_{10}$(p-value) for upregulated

(orange) and downregulated (green) genes in acute 32°C (A) or chronic 32°C (B) heat

stressed *cofilin*$^{+/-}$ embryos relative to 18°C non-stressed *cofilin*$^{+/-}$ embryos. Number of up- or down-regulated genes shown in bold.

(C, D and E). Bar plots showing $\log_2$(FC) values for upregulated (orange) or downregulated (green) genes from the highly significant ontologies: Heat stress (C); ER stress (D); and gap and pair-rule genes (Segmentation; E) for indicated conditions. Genes with no significant change in expression shown in gray.

Differential gene expression data (A-E) based on n = 5 biological replicates for chronic 32°C heat stressed WT embryos or n = 6 for all other genotypes and conditions. Significance value cut-off for genes was p < 0.05.

Cofilin knockdown embryos start from a unique transcriptomic baseline, absent any stress

How do *cofilin*^{+/-} embryos achieve a unique response when exposed to heat stress? One possibility is that *cofilin*^{+/-} and wild-type embryos start from a common transcriptomic baseline, but mount divergent responses once challenged by heat stress. Another possibility is that *cofilin*^{+/-} embryos already start with a unique transcriptome, even before encountering stress, and that sets them up for their subsequent distinct pro-survival response.

To distinguish between these possibilities, we compared our RNA-Seq data for *cofilin*^{+/-} versus wild-type embryos at the non-stressed 18°C condition. Strikingly, 948 genes were significantly upregulated and 672 downregulated in the *cofilin*^{+/-} embryos (p < 0.05; Figure 4C; Table S2). The total, 1620 genes, represents the second largest set of differentially expressed genes that we identified for any condition, ranking only behind 2477 total genes changed in wild-type embryos exposed to chronic heat stress at 32°C (Figure 2B). For the upregulated genes in non-stressed *cofilin*^{+/-} embryos, two of the most significant ontologies were related to mitochondrial processes (respiratory chain 1 and mitochondrial translation; Figures 4D and S4A; Table S4). Interestingly, several Hsp genes, including Hsp26 and Hsp68, as well as the stress-associated transcription factor, Atf-2, were upregulated, suggesting that these embryos might be sensing some type of stress even in the absence of heat exposure (Figure 4E) [98].

For the downregulated genes, several significant ontologies emerged (p ≤ 0.02), including cytoplasmic translation and four ontologies related to ER stress response (Figures 4F, 4G and S4A; Table S4). This contrasts with chronically heat-stressed wild-type embryos that

show upregulation of ER stress response genes (Figure 3D). There are some significant ontologies that relate to development, but they are largely limited to processes of the germline (Figure S4 and Table S4). Only four genes change within the core AP determination pathway (1 upregulated, 3 downregulated) and one of those is *cap-n-collar* (*cnc*), which is also associated with ER stress response (Figures 4G and 4H) [99]. Together, our results show that Cofilin knockdown, itself, leads to transcriptomic remodeling prior to any challenge by heat stress. The *cofilin$^{+/-}$* embryos start at a different baseline compared to wild-type embryos (Figure 4C-4H). This unique transcriptome supports improved survival in the absence of stress; but also prefaces a broad and potent pro-survival response when the *cofilin$^{+/-}$* embryos are challenged by either acute or chronic heat stress.
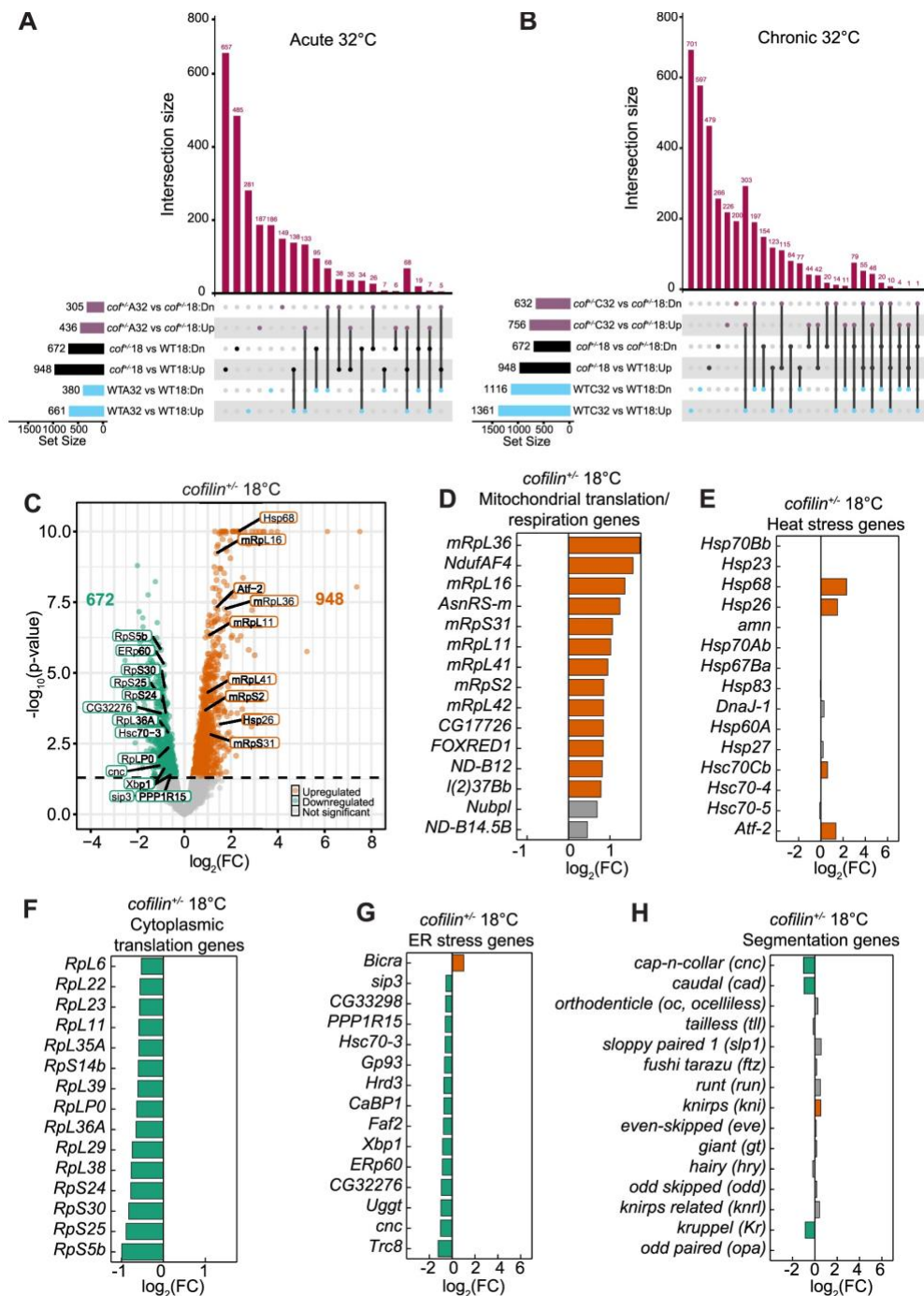
Figure 4. The *cofilin*$^{+/-}$ embryos start from a unique transcriptomic baseline prior to stress.

(A and B) UpSet plots showing intersection between up- (Up) or down- (Dn) regulated gene sets from pairwise comparisons for acute (A) or chronic (B) 32°C heat stressed embryos. Comparisons are 32°C heat-stressed *cofilin$^{+/-}$* embryos relative to 18°C non-stressed *cofilin$^{+/-}$* embryos (purple); 18°C non-stressed *cofilin$^{+/-}$* embryos relative to 18°C non-stressed wild-type (WT) embryos (black); and 32°C heat-stressed WT embryos relative to 18°C non-stressed WT embryos (cyan). Numbers in black indicate how many differentially expressed genes are included per set. Vertical black lines connecting dots indicate gene sets that intersect, and magenta bars and numbers indicate how many differentially expressed genes are shared.

(C) Volcano plot showing $\log_2$(FC) versus -$\log_{10}$(p-value) for upregulated (orange) and downregulated (green) genes in 18°C non-stressed *cofilin$^{+/-}$* embryos relative to 18°C non-stressed WT embryos. Number of up- or down-regulated genes shown in bold.

(D, E, F, G and H) Bar plots showing $\log_2$(FC) values for upregulated (orange) or downregulated (green) genes from the highly significant ontologies: Mitochondrial translation/respiration (D), Heat stress (E), Cytoplasmic translation (F), ER stress (G), and gap and pair-rule genes (Segmentation; H) for 18°C non-stressed *cofilin$^{+/-}$* embryos relative to 18°C non-stressed WT embryos. Genes with no significant change in expression shown in gray.

Differential gene expression data (A-H) based on n = 5 biological replicates for chronic 32°C heat stressed WT embryos or n = 6 for all other genotypes and conditions. Significance value cut-off for genes was p < 0.05.

Discussion

Reducing Cofilin levels or activity promotes the survival of adult mammalian cells exposed to diverse stressors and is being pursued as a therapeutic intervention for neurodegeneration, ischemic stroke and cancer [48-51,57-59]. Here, we make a parallel observation that Cofilin is a potent modulator of survival of environmentally stressed embryos. We find that, even in the absence of heat stress, *cofilin*^{+/-} embryos display a distinct transcriptomic baseline compared to wild-type embryos, and these embryos show a survival advantage over their wild-type counterparts. Once challenged by heat stress, the *cofilin*^{+/-} embryos show a striking pro-survival response that carries them through to adulthood. Our work underscores a ubiquitous role for Cofilin in cell survival and resilience, at all life stages and conserved from yeast to humans [18,21,27,50-52,56].

While Cofilin broadly influences survival, how it does so remains poorly understood. We initially hypothesized that Cofilin compromises the survival of heat stressed embryos due to actin cytoskeleton disruption and ASR. This hypothesis was premised on our own preliminary study of ASR in embryos [33], as well as from the literature on neurons, where reducing Cofilin reduces deleterious actin rod assembly under stress conditions [23,27,49]. However, when we systematically compared actin phenotypes and survival rates in embryos exposed to acute or chronic heat stress, we revised our thinking. We found that actin phenotypes, including cytoplasmic F-actin destabilization and nuclear actin rod assembly, are certainly driven by Cofilin in heat-stressed embryos [33]. However, these phenotypes persisted to notable extent even when Cofilin dosage was reduced, but these embryos, nevertheless, showed enhanced survival. Unlike the case in stressed neurons, where just a few actin rods in the cytoplasm can clearly obstruct intercellular

transport and cell function [35,36,46-48], rods in the nuclei of stressed embryos seem to be tolerated, though undoubtedly up to a limit (Figure S1I). We suggest that the actin phenotypes we have described in embryos are a symptom of heat stress, but not the sole cause of reduced survival. Thus, in the case of embryos, we do not believe that reducing Cofilin dosage rescues survival due to simple attenuation of the ASR.

Instead, our RNA-Seq analysis points to other possible mechanisms that could promote survival. For example, the transcriptomic profile of *cofilin*^{+/-} embryos in the absence of stress shows a novel interaction between Cofilin and ER stress response. Among the downregulated genes for non-stressed *cofilin*^{+/-} embryos, four ontologies relevant to ER stress response were identified. Another significant ontology, cytoplasmic translation, includes 29 ribosomal proteins, consistent with reduced ribosomal biogenesis, reduced translation, and reduced load on the ER [100,101]. In addition, the cell redox homeostasis ontology is also identified among the downregulated genes, and 67% of the genes representing this ontology are associated with ER protein folding. Together, these results argue that *cofilin*^{+/-} embryos have a lower baseline of ER stress than wild-type embryos even before exposure to heat [101,102]. After heat stress, *cofilin*^{+/-} embryos show limited changes in the expression of ER stress response genes, whereas chronically heat-stressed wild-type embryos show induction of ER stress response genes. Thus, Cofilin knockdown somehow seems to reduce ER stress across conditions. Since mitigating ER stress in early cleavage stage mammalian embryos serves as a pro-survival manipulation, this is one plausible mechanism to promote improved survival of Cofilin knockdown embryos [86,87,103].

A second possibility is that Cofilin knockdown is, itself, a stressor that helps build resilience against subsequent stress. In other words, *cofilin*^{+/-} embryos at 18°C are already experiencing mild stress due to their genotype, absent any heat exposure. This mild stress may "prime" the embryos, making them more resistant when they encounter a later more intense stress. Priming, also known as hormesis, is biology's version of "what doesn't kill you, makes you stronger". Priming is well documented in both embryos and adult organisms and can promote cellular resilience as well as organismal longevity [104-110]. Genotypic, mitochondrial, oxidative, heat and osmotic stressors can all be priming. In a simple mechanistic scenario, the priming stress serves to pre-load cells with Hsps that then aid future buffering responses [68,111-115]. Maternal preloading of transcripts and/or protein could be particularly beneficial for early embryos because they have limited capacity to respond to stress until the zygotic genome is fully activated [68,84,116,117]. Alternatively, priming can be accomplished through complex mechanisms whereby a mild stressor drives changes in gene expression that provide long-lasting adaptation to the stress (for example, mild mitochondrial dysfunction leads to nuclear-dependent remodeling of metabolism) [106,118-120]. The *cofilin*^{+/-} embryos show signs that they are responding to stress even before exposure to heat, including upregulation of Hsp26, Hsp68, and stress-associated transcription factor Atf-2, consistent with them achieving their resilient state via priming.

Whatever the pro-survival mechanism(s), *cofilin*^{+/-} embryos ultimately balance the demands of stress response and development better than their wild-type counterparts. In general, the induction of any stress response is considered antithetical to early development because the upregulation of stress response genes is expected to compete

with the normal transcriptional program needed to assemble the organism [67,71,121]. In line with this reasoning, we saw that induction of heat and ER stress response genes coincides with significant downregulation of developmental genes in heat-stressed wild-type embryos. Yet, signs of this competitive relationship were strongly diminished in *cofilin*^{+/-} embryos. Instead, *cofilin*^{+/-} embryos deploy a distinct strategy that limits induction of stress response pathways and protects against developmental perturbation. Whether reduced Cofilin dosage achieves this alternative response directly via its own activity or indirectly via actin remains an important question to address. Similarly, learning how Cofilin can control such an extensive response will be informative of its role in the survival of both embryos and adult cells.

Resource availability

Lead contact

Requests for information or resources should be directed to the lead contact, Anna Marie Sokac (asokac@illinois.edu).

Materials availability

All materials used in this study are commercially available from the sources listed in the key resources table or available upon request from the lead contact. Fly stocks are available from Bloomington *Drosophila* Stock Center (Indiana University, Bloomington, IN, USA).

Data and code availability

- Raw RNA-Seq data will be released upon publication.

- Raw mass spectrometry data is available at the PRIDE database (https://www.ebi.ac.uk/pride/) under Project Accession: PXD058671; Token: dDxylt5Mqa8L.

- Raw and analyzed imaging data is available from the lead contact upon request.

- Any additional information required to reanalyze the data in this study is available from the lead contact upon request.

Acknowledgments

Author contributions

A.M.S., N.B. and F.R. generated guiding hypotheses. N.B. and F.R. performed fly genetics. N.B. conducted imaging, image analysis, survival assays and biochemistry. F.R. conducted RNA-Seq and validation. F.R., S.N., and A.K. performed RNA-Seq and gene ontology analysis. N.B. prepared protein lysates and T.W. and T.C. performed mass spectrometry analysis. T.V.P.N. and I.G. performed post-hoc experimental correlation analysis. N.B., F.R., S.N. and T.V.P.N. generated figures and tables. A.M.S., N.B. and F.R. wrote the manuscript.

Declarations of interest

The authors declare no competing interests.

Supplemental information titles and legends

Document S1. Figures S1-S4

Table S1. Validation of RNA-Seq data by qPCR for heat stress protein (Hsp) genes.

Excel file containing additional qPCR and CPM data, related to Figures 2 and S2.

Table S2. Differentially expressed genes from RNA-Seq.

Excel file containing additional RNA-Seq data, related to Figures 2-4 and Figures S2 and S4.

Table S3. Mass spectrometry data for heat stress proteins (Hsps).

Excel file containing additional mass spectrometry data, related to Figure S3.

Table S4. Ontology analysis for differentially expressed genes identified by RNA-Seq.

Excel file containing additional gene ontology analysis (GO) data, related to Figure S2 and Figures 3-4.

Methods

EXPERIMENTAL MODEL AND SUBJECT DETAILS

Drosophila melanogaster stocks were housed on Fly Food R (Lab-Express, Ann Arbor, MI, USA). Analyses in this study focus on cellularization, corresponding to Bownes Stage 5 [83] unless otherwise noted in the Method Details.

Fly stocks and genetics

Oregon-R (OreR; BDSC#25211; Bloomington Drosophila Stock Center, Bloomington, IN, USA) was used as the wild-type stock throughout. For *cofilin*^{+/-} embryos, 3–5-day old virgin female flies from *tsr¹/CyO* (BDSC#9107; Bloomington Drosophila Stock Center), were crossed with 3–5-day old males from OreR at 25°C. F1, 3–5-day old, *tsr¹/+* virgin females were then crossed with 3–5-day old sibling males (for imaging, RNA-Seq, qPCR and biochemistry) or OreR males (for survival assays) to generate F2 embryos for experiments.

METHOD DETAILS

Embryo heat stress exposure

Embryos were harvested from apple juice agar plates affixed to collection cups as previously described in Biel 2020 [81]. To allow flies to acclimate to the starting temperature of either 18°C (for non-stressed and acute heat stress conditions) or 32°C (for the chronic heat stress condition), collection cups were incubated at 18°C for ≥ 48 hours or 32°C for

≥ 12 hours. The acclimation period at 32°C was shorter because extended incubation caused dramatically reduced fertility and increased fly death. After acclimating, embryo collections proceeded according to the schematic in Figure 1A. Specifically, for the 18°C non-stressed condition, flies were allowed to lay eggs for 2 hours, then plates were incubated at 18°C for an additional 3 hours. For the acute 32°C heat stress condition, flies were allowed to lay eggs at 18°C for 1 hour, then plates were incubated at 18°C for an additional 20 minutes, after which they were heat stressed at 32°C for 1.5 hours. For the chronic 32°C heat stress condition, flies were allowed to lay eggs at 32°C for 1 hour, then plates were incubated at 32°C for an additional 1.5 hours. Embryos were batch-collected or hand-selected as indicated per experiment.

Survival assays

Embryos with intact chorion were loosened from apple juice agar plates with distilled water and a paintbrush, then batch-collected in a cell strainer and washed thoroughly with distilled water. Embryos were transferred to a fresh agar plate with a paintbrush and hand-selected at cellularization stage under Halocarbon 27 oil (MilliporeSigma, Burlington, MA, USA).

For the larval hatching assay, selected embryos were aligned in rows on fresh agar plates, placed in a plastic box with damp paper towels, and kept at room temperature (22°C) with controlled humidity of 40% for 48 hours before empty embryo eggshells and dead embryos were counted.

For the adult eclosion assay, selected embryos were arranged on a 0.8x0.8 cm cube of agar and placed into a fresh vial of Fly Food R, embryo side up, using a pair of

offset flat-tip forceps. The vial was plugged with cotton and kept at room temperature for 14 days before the number of live adult flies and dead pupae were counted. Pupae that did not hatch after 14 days were kept for an additional 3 days to ensure any late eclosing flies were counted. Pupae that failed to hatch after 17 days were visually observed under light microscopy to confirm that they were malformed or dead.

Immunostaining and RNA fluorescence *in situ* hybridization (RNA FISH)

Embryos were batch-collected from apple juice plates by dechorionation with 3% bleach and fixed in 4% paraformaldehyde in 1X PBS according to previously published methods [64]. Fixed embryos were washed in methanol and stored at -20°C for a minimum of 24 hrs.

For immunostaining, plasma membrane furrows were detected with anti-Peanut primary antibody (1:200) (DSHB, Iowa City, IA, USA) and goat anti-mouse Alexa Fluor 488 secondary antibody (1:500) (Thermo Fisher Scientific, Waltham, MA). Nuclei were visualized with Hoechst 33342 dye (1.0 µg mL^{-1}) (Thermo Fisher Scientific).

For RNA FISH, *twist* transcript was detected using a probe set of 48 oligonucleotides (LGC BioSearch Technologies, Petaluma, CA, USA). Probe labeling with 5-TAMRA dye (Cayman Chemical, Ann Arbor, MI, USA) and hybridization proceeded according to the protocols of Xu 2015 [122]. After hybridization, nuclei were stained with Hoechst 33342 dye (1.0 µg mL^{-1}) (Thermo Fisher Scientific).

For both immunostaining and RNA FISH, embryos were mounted on slides in Aqua Poly/Mount (Polysciences, Inc., Warrington, PA, USA) and imaged using a 1.5 mm coverslip (Corning, Corning, NY, USA).

Rhodamine G-actin injections

Embryos were batch-collected from apple juice plates by dechorionation with 3% bleach at 18°C or 32°C and prepped for injection as in Biel, et al., 2020, at least 30 minutes prior to cellularization. All reagents and equipment were pre-chilled or pre-warmed to maintain temperatures to the greatest extent possible. Lyophilized rhodamine-conjugated non-muscle human platelet G-actin (G-actin[Red], Cytoskeleton Inc., Denver, CO, USA) was prepared by adding 1 µL of nuclease free water and 1 µL of freshly prepared G-buffer (5 mM Tris-HCl, 0.2 mM $CaCl_2$, 1 mM DTT, 0.2 mM ATP, pH 8.0) to 10 mg of G-actin[Red]. A glass capillary needle was loaded with 1.5 µL of the prepared G-actin[Red] and ~50 pL injected per embryo [33,81]. After injection, embryos were returned to their respective temperature conditions to incubate in humidified chambers until imaging at cellularization.

Image acquisition and presentation

Images were collected on a Zeiss LSM 880 Airyscan confocal microscope using a Plan-Apochromat 63x oil immersion objective with 1.4 numerical aperture for fixed imaging or C-Apochromat 40x water immersion objective with 1.2 numerical aperture for live imaging (Carl Zeiss, Inc., Oberkochen, Germany).

For furrows and multinucleation, images were collected as surface views from fixed wild-type or *cofilin*^{+/-} embryos at focal planes ~2-10 µm beneath the embryo surface. Images were acquired as 1024x1024 pixels/frame with 7.5879 pixels/micron for quantifying multinucleation or 15.1759 pixels/micron for presentation. For each embryo a

corresponding cross-sectional image was collected to allow measurement of the plasma membrane furrow length, which serves as a proxy for time during cellularization [79]. Images for analysis and presentation were limited to the same time window within cellularization. For presentation, color channels were adjusted separately, noise removed using the Despeckle algorithm in ImageJ/Fiji (NIH; Bethesda, MD, USA), and a Gaussian blur filter of 2 was applied in Adobe Photoshop CC (Adobe, San Jose, CA, USA).

For RNA FISH for *twist* transcripts, Z-series surface views were collected for wild-type embryos, at their ventral side in the trunk region, at focal planes ~1-6 µm beneath the embryo surface. The step size was 0.5 µm. Images were acquired as 1024x1024 pixels/frame with 5.3116 pixels/micron. Maximum intensity projections (MIPs) were created using ImageJ/Fiji. For presentation, MIPs were manually contrast adjusted, rotated, and cropped in ImageJ/Fiji. Nuclei within the ventral band region were segmented in a Layer using the Blob brush tool in Adobe Illustrator CC and color coded based on the nucleus containing 0, 1 or 2 active *twist* transcriptional foci. Individual nuclei were cropped, adjusted separately for brightness and contrast, and a Gaussian blur filter of 0.4 was applied in ImageJ/Fiji.

For FRAP of cytoplasmic furrow tips, living WT or *cofilin*^{+/-} embryos were imaged after G-actin[Red] injection at 18 ± 2°C or 32 ± 2°C in a thermal incubator. For the 32°C condition, the objective was also heated to 32 ± 2°C using an objective heater consisting of a thermal collar and temperature controller (Okolab, Sewickley, PA, USA). G-actin[Red] at furrow tips was bleached to approximately 60-70% of initial fluorescence intensity using the 561 nm laser at 100% power in cross-section views at the embryo equator. The size of the bleached box was 1.25x1.25 µm. Fluorescence recovery was tracked for 90

seconds at 1 second intervals. Images were acquired as 1024x1024 pixels/frame with 4.8177 pixels/micron, but the acquisition region was limited to 100x100 pixels to allow fast acquisition. G-actin^{Red} signal from an unbleached neighboring furrow tip was used to ascertain background bleaching due to imaging. Bleached furrows ingressed at the same rate as unbleached furrows arguing that bleaching did not cause phototoxicity [33,79]. For presentation, images were cropped, contrast adjusted, and a Gaussian blur of 0.5 was applied in Adobe Photoshop CC.

For nuclear actin rods, living wild-type or *cofilin$^{+/-}$* embryos were imaged at 18 ± 2°C or 32 ± 2°C in a thermal incubator as described for furrow tip FRAP. For the 32°C condition, the objective was also heated to 32 ± 2°C using an objective heater. Z-series surface views were collected at ~2-10 µm beneath the embryo's surface, within the top two-thirds of the nuclei. Images were acquired as 1024x1024 pixels/frame with 3.6133 pixels/micron for counting rods or 9.6355 pixels/micron for quantifying rod morphology. For presentation, actin rod images were adjusted for brightness, cropped in ImageJ/Fiji and a Gaussian blur filter of 0.75 was applied in Adobe Photoshop CC.

For FRAP of actin rods, living WT or *cofilin$^{+/-}$* embryos were imaged after G-actin^{Red} injection as described for furrow tip FRAP with the following exceptions: Actin rods were imaged in surface views at ~2-10 µm beneath the embryo's surface. The size of the bleached box was 2x2 µm. Fluorescence recovery was tracked for 60 seconds at 1-2 second intervals. Images were acquired as 1024x1024 pixels/frame with 4.8177 pixels/micron, but the acquisition region was limited to 200x200 pixels for faster acquisition. Cytoplasmic G-actin^{Red} signal from an unbleached neighboring region was used to ascertain background bleaching due to imaging. For presentation, images were

cropped, contrast adjusted, and a Gaussian blur of 0.5 was applied in Adobe Photoshop CC.

RNA Sequencing

Embryos were batch-collected from apple juice plates as for the survival assays, using water, at 18°C or 32°C. Reagents and equipment were pre-chilled or pre-warmed to maintain temperatures to the greatest extent possible. Embryos were transferred to a fresh agar plate with a paintbrush and cellularization stage embryos selected under Halocarbon 27 oil (MilliporeSigma). Selected embryos were snap-frozen using liquid nitrogen and stored at -80°C.

RNA was extracted from six biological replicates of wild-type and *cofilin*$^{+/-}$ embryos per temperature condition. In addition, two more biological replicates of wild-type fly embryos were included as batch controls during collection of *cofilin*$^{+/-}$ embryos. RNA was extracted using the RNeasy Plus Micro Kit (Qiagen, Germantown, PA, USA). RNA quality was confirmed by measuring the RNA Quality Number & 28S/18S rRNA ratio using AATI Fragment Analyzer (Advanced Analytics, Ames, IA, USA).

Stranded RNAseq libraries were generated by the DNA Services Laboratory (Roy J. Carver Biotechnology Center, University of Illinois at Urbana-Champaign) utilizing the KAPA mRNA HyperPrep Kit (Roche, Indianapolis, IN, USA). Specifically, 200 ng of total RNA per sample was used to isolate PolyA+ RNA which was fragmented at 94°C for 4 minutes, and random hexamers and SuperScript II Reverse Transcriptase (Invitrogen / Thermo Fisher Scientific) were used for first strand cDNA synthesis. Double-stranded DNA was ligated to universal adaptor, 3'-end A-tailed, blunt-ended and amplified by PCR

for 12 cycles using Twist unique dual index primers (Twist Bioscience, San Francisco, CA, USA). Final libraries were diluted to a final concentration of 5nM.

Libraries were sequenced by the DNA Services Laboratory as 150 bp, paired-end reads using the Illumina NovaSeq 6000 SP flow cell (Illumina, San Diego, CA, USA). Sequencing analysis produced .bcl files which were transformed into adaptor-trimmed and demultiplexed fastq format files using bcl2fastq v2.20 Conversion Software (Illumina).

qPCR

Wild-type embryos were collected for three biological replicates per condition, and RNA was extracted as for RNA-Seq. Total RNA samples of 300ng were reverse transcribed using random hexamer primers and the iScript Select cDNA Synthesis Kit (Bio-Rad, Hercules, CA, USA). cDNA was diluted 1:5 and real-time qPCR performed on the Applied Biosystems StepOnePlus Real-Time PCR system using TaqMan™ Fast Advanced Master Mix and TaqMan Gene Expression Assays (Applied Biosystems / Thermo Fisher Scientific). Predesigned TaqMan Gene Expression Assays (Thermo Fisher Scientific) were used for *Hsp23* (Assay ID: Dm01822473_s1), *Hsp26* (Assay ID: Dm01822452_s1), *Hsp68* (Assay ID: Dm02151262_s1), *Hsc70-4* (Assay ID: Dm02153823_s1), *Hsp83* (Assay ID: Dm02362342_s1), and *DnaJ-1* (Assay ID: Dm01832926_s1). A custom TaqMan Gene Expression Assay (Thermo Fisher Scientific) was used for *Hsp70*. The gene *roadblock* (*robl*; Thermo Fisher Scientific, Catalog# 4351372, Assay ID: Dm01821522_g1) served as a reference control to normalize C_T values per Hsp gene. The *robl* gene was selected due to its stable expression across experimental groups in the RNA-Seq experiments.

Western Blotting

Wild-type and *cofilin⁺ᐟ⁻* embryos were collected as for RNA-Seq. Three biological

replicates of 200 embryos per condition were homogenized by hand on ice in lysis buffer

(150 µL 0.05 M Tris-HCl pH 8.0, 0.15 M KCl, 0.05 M EDTA, 0.5% NP-40, 1X protease

inhibitor cocktail (Thermo Fisher Scientific)) in low-protein retention microcentrifuge tubes

(Thermo Fisher Scientific) using sterile plastic pestles. Embryo debris was pelleted, and

soluble lysate collected. Protein concentration was determined by BCA assay (Thermo

Fisher Scientific) and lysates diluted with lysis buffer to obtain the same concentration

between samples. Lysates were boiled with 1x SDS-PAGE reducing buffer (62.5 mM Tris-

HCl pH 6.8, 2% SDS, 10% glycerol, 41.6 mM DTT, 0.01% bromophenol blue) and run at

a concentration of 5 µg per lane through 12% hand cast bis-acrylamide separating gels.

Protein was transferred to 0.2 µm nitrocellulose (Bio-Rad) and probed with 1:200 mouse

anti-β-actin (Santa Cruz Biotechnology, Dallas, TX, USA) and 1:5000 rabbit anti-*Dm*-

Cofilin [33], followed by goat anti-mouse or goat anti-rabbit HRP secondary antibodies

(Jackson ImmunoResearch, West Grove, PA, USA).

Mass spectrometry sample preparation

Embryo collection and protein lysate preparation followed the same methodology

as for Western Blotting with the following exceptions: Approximately 62 µg of protein was

loaded per gel lane and run through pre-made 4-20% bis-polyacrylamide SDS-PAGE

separating gels (Bio-Rad) beside pre-stained molecular weight standards

(MilliporeSigma). Lysates were loaded with empty lanes separating them to prevent

contamination between samples. Gels were fixed and stained with QC Colloidal Coomassie G-250 stain according to the manufacturer's Quick Stain protocol (Bio-Rad) and gel regions between the 17-35 kDa and 50-100 kDa molecular weight markers were cut out per lane with a clean razor blade. Gel pieces were stored and shipped in low-protein retention tubes at 4°C.

Gel pieces were washed with 50 mM ammonium Bicarbonate (NH_4HCO_3; Acros Organics / Thermo Fisher Scientific) in 50% acetonitrile (ACN; Fisher Scientific, Hampton, NH, USA) and dehydrated with 100% ACN. The gel pieces were reduced with 10 mM Tris(2-carboxyethyl)phosphine (TECP; MilliporeSigma) at 55°C for 30 minutes, followed by alkylation with 10 mM 2-chloroacetamide (CAA; MilliporeSigma) for 45 minutes at room temperature in the dark. Then, gel pieces were dehydrated in ACN and dried prior to overnight digestion with a 20 ng/µl trypsin (Thermo Fisher Scientific) solution prepared in 50 mM NH_4HCO_3. Digestion was halted with 5% formic acid (FA; Fisher Scientific) and the solution transferred to clean tubes. Peptides were extracted from the gel pieces by incubation with 0.1% FA in 50% ACN for 15 minutes, and the extracted solution was combined with the previous digestion solution. Digested peptides were desalted using ZipTip pipette tips (MilliporeSigma) according to the manufacturer's protocol. After desalting, peptides were dried and reconstituted in water containing 0.2% FA and 2% ACN for subsequent LC-MS/MS analysis.

Mass spectrometry analysis

Mass spectrometry was performed with a Vanquish Neo UHPLC system (Thermo Fisher Scientific) coupled to an Orbitrap Eclipse Tribrid mass spectrometer (Thermo Fisher Scientific). Peptides were separated on an Aurora UHPLC Column (25 cm × 75 μm, 1.7 μm C18, AUR3-25075C18-TS; Ion Opticks, Collingwood, VIC, Australia) with a flow rate of 0.35 μL/min for a total duration of 43 min and ionized at 1.6 kV in the positive ion mode. The gradient was composed of 6% solvent B (3 min), 6-25% B (20 min), 25-40% B (7 min), and 40–98% B (13 min); solvent A: 0.1% (v/v) FA; solvent B: 0.1% (v/v) FA/80% (v/v) ACN. MS1 scans were acquired at the resolution of 120,000 from 350 to 2,000 m/z, AGC target 1e6, and maximum injection time 50 milliseconds. MS2 scans were acquired in the ion trap using fast scan rate on precursors with 2-7 charge states and quadrupole isolation mode (isolation window: 1.2 m/z) with higher-energy collisional dissociation (HCD, 30%) activation type. Dynamic exclusion was set to 30 seconds. The temperature of ion transfer tube was 300°C and the S-lens RF level was set to 30.

QUANTIFICATIONS AND STATISTICAL ANALYSIS

Student's t-tests were performed using custom code from MATLAB's Statistics and Machine Learning Toolbox (Mathworks, Natick, MA, USA). χ^2-contingency analysis was performed using GraphPad QuickCalcs (GraphPad, San Diego, CA, USA). Specific p-values and n-values can be found within the figures and their legends. For imaging data, comparisons with $p < 0.05$ were considered significant. For RNA-Seq, genes following the significance cutoff clearance: $p < 0.05$ were considered differentially expressed (up- or down-regulated). For identifying important ontologies, GO Biological Processes following the significance cutoff clearance: $p \leq 0.02$ were considered. All plots were generated using custom codes in MATLAB, except for the volcano and UpSet plots which were generated using R (Vienna, Austria) packages 'ggplot2' and 'UpSetR', respectively. Final plots and figures were assembled using Adobe Illustrator CC.

Actin rod quantification

To quantify the percent embryos displaying actin rods in Figure 1G, surface view images with ≥ 250 visible nuclei were scored manually, and the presence of rods was defined as bright G-actin[Red] streaks visible within the nuclei, approximately 0.1-0.2 µm in diameter and present in at least two contiguous focal planes.

To quantify rods per nucleus in Figure 1H, rods were identified manually in ImageJ/Fiji from a 256x256 pixel region of the raw Z-stack (~80-130 nuclei counted per embryo), scrolling through multiple focal planes to assure accurate counting. Rods and

nuclei were then counted individually using the Selection and Measure tools, and the ratio of rods/nuclei calculated per embryo.

To quantify rod diameters in Figure S1E, five nuclei representing four quadrants and a central region of a 512x512 pixel cropped image from the raw Z-stack were chosen. The diameters of all rods in each nucleus were measured manually using the Line and Measure tools in ImageJ/Fiji. If one nucleus contained more than one rod, the mean diameter for that nucleus was calculated. The five means per embryo were plotted as individual data points in the final figure.

To quantify FRAP for rods in Figure S1G, a 2x2 µm box was drawn around the bleached region and the mean fluorescence intensity manually measured for each frame using ImageJ/Fiji. Fluorescence in an unbleached cytoplasmic region was tracked to account for photobleaching effects using Method 1 described in Figard *et al.*, 2019 [33]. MATLAB was used to generate the recovery fit curves.

For all rod experiments, data shown is based on n ≥ 3 independent biological replicates.

Multinucleation quantification

To quantify the percent embryos with multinucleation in Figure S1C, raw z-stack images were scored manually for the presence of multinucleation (≥100 nuclei per image), scanning through multiple focal planes to assure accurate counting.

To quantify the ratio of multinucleate cells/total nuclei in Figure S1D, the number of multinucleated cells and total nuclei in the frame of each image were counted manually

in ImageJ/Fiji using the Pencil and Multi-point selection tools. Segmented images were generated from the raw images manually using the Pen tool in Adobe Illustrator CC.

For all multinucleation experiments, data shown is based on n ≥ 3 independent biological replicates.

RNA FISH quantification

To quantify the number of *twist* transcriptional foci per nucleus in Figures 2D and E, MIPs were scored manually. Nuclei within the ventral band tissue were counted as "on" if they contained one or two bright foci that were at least 0.2 μm^2 in diameter. The total number of nuclei were counted in the ventral tissue band and the percent nuclei with 0, 1 or 2 foci calculated. Segmented images were created manually in Adobe Illustrator CC.

Data shown is based on n = 3 independent biological replicates.

RNA-Seq analysis

Raw RNA-Seq data was checked for read quality using FastQC (version 0.11.9; Babraham Bioinformatics, Cambridge, UK). Reads were aligned to the *Drosophila* genome from FlyBase (FASTA: dmel-all-chromosome-r6.50.fasta, GTF: dmel-all-r6.50.gtf) using STAR (version 2.7.11b) [123]. Sorted bam files were then indexed using SAMtools index. Htseq (version 2.0.2) [124] was used to count the number of reads aligned to each gene. Read normalization, variance estimation, and pairwise differential expression analysis was performed using the Bioconductor package EdgeR (version 3.40.2) [125]. Gene set enrichment analysis was performed with PANGEA using the gene

set "Direct GO Biological Processes" [85]. Genes that were expressed (CPM > 1) in at least 2 replicates across both the groups served as background.

qPCR analysis and RNA-Seq validation

Relative gene expression values for wild-type embryos for *Hsp23*, *Hsp26*, *Hsp68*, *Hsp70, Hsp83*, *Hsc70-4* and *DnaJ-1* were calculated as $2^{-\Delta\Delta C_T}$ values from qPCR results, as described in Livak and Schmittgen, 2001 and Schmittgen and Livak, 2008 [126,127]. Specifically, C_T values for individual experimental replicates were normalized by subtracting the corresponding reference gene *robl* C_T value to obtain ΔC_T. $\Delta\Delta C_T$ values for each experimental replicate were obtained by subtracting each replicate's ΔC_T value from the mean ΔC_T control value, which was averaged from the three experimental replicates for the 18°C non-stressed wild-type control sample.

For comparison and validation of RNA-Seq data with qPCR data, as represented in Figure S2A and Table S1, the average fold change of counts per million (CPM) of RNA abundance was compared to the average relative gene expression value ($-\Delta\Delta C_T$) from qPCR for each Hsp gene for acute 32°C and chronic 32°C heat stressed wild-type embryos. Average CPM fold changes for each gene were calculated by dividing the average CPM value for either acute 32°C or chronic 32°C by the average CPM value for 18°C non-stressed wild-type embryos. Data was plotted using MATLAB and the best fit curve was estimated using the Curve Fitting Toolbox app. Two additional and independent analyses methods yielded similar plots to Figure S2A with adjusted R values > 0.72 for all best fit curves.

Mass spectrometry data analysis

MS2 fragmentation spectra were searched with Proteome Discoverer SEQUEST (version 2.5, Thermo Fisher Scientific) against *in silico* tryptic digested Uniprot *Drosophila melanogaster* (UP000000803). The maximum missed cleavages were set to 2. Dynamic modifications were set to oxidation on methionine (M, +15.995 Da) and protein N-terminal acetylation (+42.011 Da). Carbamidomethylation on cysteine residues (C, +57.021 Da) was set as a fixed modification. The maximum parental mass error was set to 10 ppm, and the MS2 mass tolerance was set to 0.6 Da. The false discovery threshold was set strictly to 0.01 using the Percolator Node validated by q-value. The relative abundance of parental peptides was calculated by integration of the area under the curve of the MS1 peaks using the Minora LFQ node. Mass spectrometry proteomics data were deposited to the ProteomeXchange Consortium via the PRIDE partner repository [128] with the dataset identifier PXD058671.

Bootstrapping analysis

Error analysis and fitting in Figures S1H, S1I, S2F and S2G were performed by bootstrapping as follows: In each bootstrapping iteration, for each of the six conditions (two genotypes: wild-type and *cofilin*^{+/-}; three conditions: 18°C non-stressed, acute 32°C heat-stressed and chronic 32°C heat-stressed), the values of the percent larval survival (from the biological replicates) were randomly drawn with replacement to generate a bootstrap sample. Random drawing was implemented using the MATLAB 'datasample' function. The mean percent values of larval survival for the six conditions were calculated using the corresponding bootstrap sample of each condition. Using the same procedure,

we calculated the mean values of the number of multinucleate cells per total nuclei; the number of rods per nucleus; the percentage of gap and pair-rule genes with differential expression; and the sum of the $\log_2$(FC) in gap and pair-rule gene expression. Next, linear regression was performed by fitting the equation $y = ax+b$ (where y is the mean percent larval survival and x is the mean of one of the other four variables) to the paired values of the six conditions; these paired values and the resulting estimates of the fitting parameters a and b are specific to a given bootstrapping iteration. We repeated this bootstrapping procedure for $n = 1000$ iterations. The best-fit values and standard errors of the mean of a and b were calculated from the mean and standard deviations of the estimates of a and b across all iterations. The paired mean values for the six conditions were plotted with the regression line (black), calculated using the best-fit values of a and b. The uncertainty in the regression line (gray shading), was calculated as the standard error propagated from the standard of a and b.

The same bootstrapping procedure was performed for the collapse plot in Figure S2H, using the following fitting equation: $y = y_0 \times (1-(x/x_c)^\alpha)$. In this equation, y is the mean percent larval survival, x is the mean of one of the other four variables, y_0 is the y-intercept (the y value when $x=0$), x_c is the x-intercept (the x value when $y=0$), and α is the critical exponent.

Densitometry

Images of processed Western Blots for Figure S1J were acquired at 300 dpi resolution using the iBright CL1000 instrument and imaging software (Thermo Fisher Scientific). Images were inverted and converted to 8-bit in ImageJ/Fiji and quantified in

Adobe Photoshop CC using the Rectangular Marquee tool. For each blot, the integrated intensities per band were normalized against the 18°C wild-type β-actin band so results could be related between biological replicates.

Mean Cofilin protein level in *cofilin*^{+/-} embryos is based on n = 3 independent biological replicates.

Key Resources Table

REAGENT or RESOURCE	SOURCE	IDENTIFIER
Antibodies		
Affinipure Goat Anti-Mouse IgG(H+L) horseradish peroxidase-conjugated secondary antibody	Jackson ImmunoResearch	Cat#115-035-003 RRID:AB_10015289
Affinipure Goat Anti-Rabbit IgG(H+L) horseradish peroxidase-conjugated secondary antibody	Jackson ImmunoResearch	Cat#111-035-003 RRID:AB_2313567
Anti-β-actin, Mouse monoclonal	Santa Cruz Biotechnology	Cat#sc-47778 RRID:AB_626632
Anti-*Dm* Cofilin, Rabbit polyclonal	Figard et al., 2019 [33]	Cat#Sokac_Dm_Cofilin; RRID:AB_3669047
Anti-Peanut, Mouse monoclonal	Developmental Studies Hybridoma Bank (DSHB)	Cat#4C9H4-c; RRID:AB_528429
Goat anti-mouse IgG (H+L) cross-adsorbed secondary antibody, Alexa Fluor^{TM} 488	Invitrogen / Thermo Fisher Scientific	Cat#A-11001 RRID:AB_2534069
Chemicals, peptides, and recombinant proteins		
2-Chloroacetamide (CAA)	MilliporeSigma	Cat#22790
4-20% Mini-PROTEAN TGX Pre-cast protein gels, 10-well, 30 uL	Bio-Rad	Cat#4561093
5-Carboxytetramethylrhodamine (5-TAMRA)	Cayman Chemical	Cat#34598
Acetonitrile, Optima, LC/MS Grade, Fisher Chemical (ACN)l	Acros Organics / Fisher Scientific	Cat#A9554
Actin protein, human platelet, non-muscle, rhodamine-conjugated (G-actin^{Red})	Cytoskeleton, Inc.	Cat#APHR-C
Ammonium bicarbonate, 99% (NH_4HCO_3)	Thermo Fisher Scientific	Cat#393212500
Aqua-Poly/Mount	Polysciences	Cat#18606-20
BLUeye Prestained Protein Ladder	MilliporeSigma	Cat#94964-500UL
ECL Western Blotting Substrate	Pierce / Thermo Fisher Scientific	Cat#32209
Formic acid (FA)	Fisher Scientific	Cat#A11750
Halocarbon 27 oil	MilliporeSigma	Cat#H8773-100ML
Halocarbon 700 oil	MilliporeSigma	Cat#H8898-100ML
Hoechst 33342	Invitrogen / Thermo Fisher Scientific	Cat#H3570
Molecular Biology Grade Water	Corning	Cat#46-000-CM
Protease Inhibitor Mini Tablets, EDTA-free	Pierce / Thermo Fisher Scientific	Cat#A32955
QC Colloidal Coomassie Stain	Bio-Rad	Cat#1610803
SuperScript II Reverse Transcriptase	Invitrogen / Thermo Fisher Scientific	Cat#18064071
TaqMan Fast Advanced Master Mix	Thermo Fisher Scientific	Cat#4444557
Tris(2-carboxyethyl)phosphine hydrochloride (TECP)	MilliporeSigma	Cat#C4706
Trypsin	Thermo Fisher Scientific	Cat#90305

Critical commercial assays		
BCA Assay	Pierce / Thermo Fisher Scientific	Cat#23235
iScript Select cDNA Synthesis Kit	Bio-Rad	Cat#1708897
KAPA mRNA HyperPrep Kit	Roche	Cat#KK8581
RNeasy Plus Micro Kit	Qiagen	Cat#74034
Deposited data		
Raw RNA-Seq data	This paper	NIH BioProject#: PRJNA1196936
Raw mass spectrometry data	This paper	PRIDE Project Accession#: PXD058671; Token: dDxylt5Mqa8L
Experimental models: Organisms/strains		
tsr^1/CyO (cofilin$^{+/-}$)	Bloomington Drosophila Stock Center	Cat#9107; RRID:BDSC_9107
Oregon-R-modENCODE (modENCODE OreR)	Bloomington Drosophila Stock Center	Cat#25211; RRID:BDSC_25211
Oligonucleotides		
LGC BioSearch Technologies Stellaris twist Custom RNA FISH probe set, conjugated to TAMRA dye	LGC BioSearch Technologies	This paper; Sequences available upon request
Predesigned TaqMan Gene Expression Assay for Hsp83	Thermo Fisher Scientific	Cat#4448892 Assay ID: Dm02362342
Custom TaqMan Gene Expression Assay for Hsp70	Thermo Fisher Scientific	Cat#4331348, Assay ID: APWC647
Predesigned TaqMan Gene Expression Assay for Hsp68	Thermo Fisher Scientific	Cat#4448892 Assay ID: Dm02151262_s1
Predesigned TaqMan Gene Expression Assay for Hsp26	Thermo Fisher Scientific	Cat#4448892 Assay ID: Dm01822452_s1
Predesigned TaqMan Gene Expression Assay for Hsp23	Thermo Fisher Scientific	Cat#4448892 Assay ID: Dm01822473_s1
Predesigned TaqMan Gene Expression Assay for DNAJ-1	Thermo Fisher Scientific	Cat#4448892 Assay ID: Dm01832926_s1
Predesigned TaqMan Gene Expression Assay for robl	Thermo Fisher Scientific	Cat#4448892 Assay ID: Dm01821522_g1
Predesigned TaqMan Gene Expression Assay for Hsc70-4	Thermo Fisher Scientific	Cat#4448892 Assay ID: Dm02153823_s1
Software and algorithms		
Adobe Illustrator CC	Adobe	https://www.adobe.com/creativecloud.html
Adobe Photoshop CC	Adobe	https://www.adobe.com/creativecloud.html

IBM SPSS Statistics 29.0.2.0	International Business Machines Corporation	https://www.ibm.com/products/spss-statistics
ImageJ / FIJI	NIH	https://fiji.sc
MATLAB	Mathworks	https://www.mathworks.com/products/matlab.html
R	R Core Team	https://www.R-project.org/
Other		
Aurora UHPLC Column 25 cm×75 µm, 1.7 µm C18	Ion Opticks	Cat#AUR3-25075C18-TS
Cover glass, 24x50 mm, 1 ½ mm thickness	Corning	Cat#2980-245
Fly food R	LabExpress	https://lab-express.com/flyfoodsupplies.htm
Heated incubator	PHC Corporation of America	Cat#MIR-154-PA
Objective heater and temperature controller	Okolab	Cat#H401-T-Penny
Offset flat-tip forceps	Thermo Fisher Scientific	Cat#16-100-116
Snap cap low retention microcentrifuge tubes	Thermo Fisher Scientific	Cat#3448
ZipTip pipette tips	MilliporeSigma	Cat#ZTC18S096

References

1.   Bravo-Cordero, J.J., Magalhaes, M.A., Eddy, R.J., Hodgson, L., and Condeelis, J. (2013). Functions of cofilin in cell locomotion and invasion. Nat Rev Mol Cell Biol *14*, 405-415. 10.1038/nrm3609.

2.   Andrianantoandro, E., and Pollard, T.D. (2006). Mechanism of actin filament turnover by severing and nucleation at different concentrations of ADF/cofilin. Mol Cell *24*, 13-23. 10.1016/j.molcel.2006.08.006.

3.   McCullough, B.R., Blanchoin, L., Martiel, J.L., and De la Cruz, E.M. (2008). Cofilin increases the bending flexibility of actin filaments: implications for severing and cell mechanics. J Mol Biol *381*, 550-558. 10.1016/j.jmb.2008.05.055.

4.   Bamburg, J.R., Minamide, L.S., Wiggan, O., Tahtamouni, L.H., and Kuhn, T.B. (2021). Cofilin and Actin Dynamics: Multiple Modes of Regulation and Their Impacts in Neuronal Development and Degeneration. Cells *10*. 10.3390/cells10102726.

5.   Chua, B.T., Volbracht, C., Tan, K.O., Li, R., Yu, V.C., and Li, P. (2003). Mitochondrial translocation of cofilin is an early step in apoptosis induction. Nat Cell Biol *5*, 1083-1089. 10.1038/ncb1070.

6.   Klamt, F., Zdanov, S., Levine, R.L., Pariser, A., Zhang, Y., Zhang, B., Yu, L.R., Veenstra, T.D., and Shacter, E. (2009). Oxidant-induced apoptosis is mediated by oxidation of the actin-regulatory protein cofilin. Nat Cell Biol *11*, 1241-1246. 10.1038/ncb1968.

7.   Goode, B.L., Eskin, J., and Shekhar, S. (2023). Mechanisms of actin disassembly and turnover. J Cell Biol *222*. 10.1083/jcb.202309021.

8.   Abe, H., Nagaoka, R., and Obinata, T. (1993). Cytoplasmic localization and nuclear transport of cofilin in cultured myotubes. Exp Cell Res *206*, 1-10. 10.1006/excr.1993.1113.

9.   Blanchoin, L., and Pollard, T.D. (1998). Interaction of actin monomers with Acanthamoeba actophorin (ADF/cofilin) and profilin. J Biol Chem *273*, 25106-25111. 10.1074/jbc.273.39.25106.

10. Carlier, M.F., Laurent, V., Santolini, J., Melki, R., Didry, D., Xia, G.X., Hong, Y., Chua, N.H., and Pantaloni, D. (1997). Actin depolymerizing factor (ADF/cofilin) enhances the rate of filament turnover: implication in actin-based motility. J Cell Biol *136*, 1307-1322. 10.1083/jcb.136.6.1307.

11. Iida, K., Matsumoto, S., and Yahara, I. (1992). The KKRKK sequence is involved in heat shock-induced nuclear translocation of the 18-kDa actin-binding protein, cofilin. Cell Struct Funct *17*, 39-46. 10.1247/csf.17.39.

12. Maciver, S.K., and Weeds, A.G. (1994). Actophorin preferentially binds monomeric ADP-actin over ATP-bound actin: consequences for cell locomotion. FEBS Lett *347*, 251-256. 10.1016/0014-5793(94)00552-4.

13. Dopie, J., Rajakyla, E.K., Joensuu, M.S., Huet, G., Ferrantelli, E., Xie, T., Jaalinoja, H., Jokitalo, E., and Vartiainen, M.K. (2015). Genome-wide RNAi screen for nuclear actin reveals a network of cofilin regulators. J Cell Sci *128*, 2388-2400. 10.1242/jcs.169441.

14. Dopie, J., Skarp, K.P., Rajakyla, E.K., Tanhuanpaa, K., and Vartiainen, M.K. (2012). Active maintenance of nuclear actin by importin 9 supports transcription. Proc Natl Acad Sci U S A *109*, E544-552. 10.1073/pnas.1118880109.

15. Obrdlik, A., and Percipalle, P. (2011). The F-actin severing protein cofilin-1 is required for RNA polymerase II transcription elongation. Nucleus *2*, 72-79. 10.4161/nucl.2.1.14508.

16. Gellert, M., Hanschmann, E.M., Lepka, K., Berndt, C., and Lillig, C.H. (2015). Redox regulation of cytoskeletal dynamics during differentiation and de-differentiation. Biochim Biophys Acta *1850*, 1575-1587. 10.1016/j.bbagen.2014.10.030.

17. Klemke, M., Wabnitz, G.H., Funke, F., Funk, B., Kirchgessner, H., and Samstag, Y. (2008). Oxidation of cofilin mediates T cell hyporesponsiveness under oxidative stress conditions. Immunity *29*, 404-413. 10.1016/j.immuni.2008.06.016.

18. Madineni, A., Alhadidi, Q., and Shah, Z.A. (2016). Cofilin Inhibition Restores Neuronal Cell Death in Oxygen-Glucose Deprivation Model of Ischemia. Mol Neurobiol *53*, 867-878. 10.1007/s12035-014-9056-3.

19. Samstag, Y., John, I., and Wabnitz, G.H. (2013). Cofilin: a redox sensitive mediator of actin dynamics during T-cell activation and migration. Immunol Rev *256*, 30-47. 10.1111/imr.12115.

20. Wabnitz, G.H., Goursot, C., Jahraus, B., Kirchgessner, H., Hellwig, A., Klemke, M., Konstandin, M.H., and Samstag, Y. (2010). Mitochondrial translocation of oxidized cofilin induces caspase-independent necrotic-like programmed cell death of T cells. Cell Death Dis *1*, e58. 10.1038/cddis.2010.36.

21. Woo, J.A., Jung, A.R., Lakshmana, M.K., Bedrossian, A., Lim, Y., Bu, J.H., Park, S.A., Koo, E.H., Mook-Jung, I., and Kang, D.E. (2012). Pivotal role of the RanBP9-

cofilin pathway in Abeta-induced apoptosis and neurodegeneration. Cell Death Differ *19*, 1413-1423. 10.1038/cdd.2012.14.

22. Xiang, S.Y., Ouyang, K., Yung, B.S., Miyamoto, S., Smrcka, A.V., Chen, J., and Heller Brown, J. (2013). PLCepsilon, PKD1, and SSH1L transduce RhoA signaling to protect mitochondria from oxidative stress in the heart. Sci Signal *6*, ra108. 10.1126/scisignal.2004405.

23. Bamburg, J.R., and Bernstein, B.W. (2016). Actin dynamics and cofilin-actin rods in alzheimer disease. Cytoskeleton (Hoboken) *73*, 477-497. 10.1002/cm.21282.

24. Kanellos, G., and Frame, M.C. (2016). Cellular functions of the ADF/cofilin family at a glance. J Cell Sci *129*, 3211-3218. 10.1242/jcs.187849.

25. Ashworth, S.L., Southgate, E.L., Sandoval, R.M., Meberg, P.J., Bamburg, J.R., and Molitoris, B.A. (2003). ADF/cofilin mediates actin cytoskeletal alterations in LLC-PK cells during ATP depletion. Am J Physiol Renal Physiol *284*, F852-862. 10.1152/ajprenal.00210.2002.

26. Ben Zablah, Y., Merovitch, N., and Jia, Z. (2020). The Role of ADF/Cofilin in Synaptic Physiology and Alzheimer's Disease. Front Cell Dev Biol *8*, 594998. 10.3389/fcell.2020.594998.

27. Chen, B., Lin, W., Qi, W., Li, S., Hong, Z., and Zhao, H. (2020). Cofilin Inhibition by Limk1 Reduces Rod Formation and Cell Apoptosis after Ischemic Stroke. Neuroscience *444*, 64-75. 10.1016/j.neuroscience.2020.07.019.

28. Goebel, H.H., Anderson, J.R., Hubner, C., Oexle, K., and Warlo, I. (1997). Congenital myopathy with excess of thin myofilaments. Neuromuscul Disord *7*, 160-168. 10.1016/s0960-8966(97)00441-0.

29. Mai, N., Wu, L., Uruk, G., Mocanu, E., and Swanson, R.A. (2024). Bioenergetic and excitotoxic determinants of cofilactin rod formation. J Neurochem *168*, 899-909. 10.1111/jnc.16065.

30. Munsie, L., Caron, N., Atwal, R.S., Marsden, I., Wild, E.J., Bamburg, J.R., Tabrizi, S.J., and Truant, R. (2011). Mutant huntingtin causes defective actin remodeling during stress: defining a new role for transglutaminase 2 in neurodegenerative disease. Hum Mol Genet *20*, 1937-1951. 10.1093/hmg/ddr075.

31. Wurz, A.I., Schulz, A.M., O'Bryant, C.T., Sharp, J.F., and Hughes, R.M. (2022). Cytoskeletal dysregulation and neurodegenerative disease: Formation, monitoring, and inhibition of cofilin-actin rods. Front Cell Neurosci *16*, 982074. 10.3389/fncel.2022.982074.

32. Davis, R.C., Marsden, I.T., Maloney, M.T., Minamide, L.S., Podlisny, M., Selkoe, D.J., and Bamburg, J.R. (2011). Amyloid beta dimers/trimers potently induce cofilin-actin rods that are inhibited by maintaining cofilin-phosphorylation. Mol Neurodegener *6*, 10. 10.1186/1750-1326-6-10.

33. Figard, L., Zheng, L., Biel, N., Xue, Z., Seede, H., Coleman, S., Golding, I., and Sokac, A.M. (2019). Cofilin-Mediated Actin Stress Response Is Maladaptive in Heat-Stressed Embryos. Cell Rep *26*, 3493-3501 e3494. 10.1016/j.celrep.2019.02.092.

34. Ishikawa-Ankerhold, H.C., Kurzbach, S., Kinali, A.S., and Muller-Taubenberger, A. (2021). Formation of Cytoplasmic Actin-Cofilin Rods is Triggered by Metabolic Stress and Changes in Cellular pH. Front Cell Dev Biol *9*, 742310. 10.3389/fcell.2021.742310.

35.   Maloney, M.T., Minamide, L.S., Kinley, A.W., Boyle, J.A., and Bamburg, J.R. (2005). Beta-secretase-cleaved amyloid precursor protein accumulates at actin inclusions induced in neurons by stress or amyloid beta: a feedforward mechanism for Alzheimer's disease. J Neurosci *25*, 11313-11321. 10.1523/JNEUROSCI.3711-05.2005.

36.   Minamide, L.S., Striegl, A.M., Boyle, J.A., Meberg, P.J., and Bamburg, J.R. (2000). Neurodegenerative stimuli induce persistent ADF/cofilin-actin rods that disrupt distal neurite function. Nat Cell Biol *2*, 628-636. 10.1038/35023579.

37.   Bernstein, B.W., Shaw, A.E., Minamide, L.S., Pak, C.W., and Bamburg, J.R. (2012). Incorporation of cofilin into rods depends on disulfide intermolecular bonds: implications for actin regulation and neurodegenerative disease. J Neurosci *32*, 6670-6681. 10.1523/JNEUROSCI.6020-11.2012.

38.   Huang, T.Y., Minamide, L.S., Bamburg, J.R., and Bokoch, G.M. (2008). Chronophin mediates an ATP-sensing mechanism for cofilin dephosphorylation and neuronal cofilin-actin rod formation. Dev Cell *15*, 691-703. 10.1016/j.devcel.2008.09.017.

39.   Minamide, L.S., Maiti, S., Boyle, J.A., Davis, R.C., Coppinger, J.A., Bao, Y., Huang, T.Y., Yates, J., Bokoch, G.M., and Bamburg, J.R. (2010). Isolation and characterization of cytoplasmic cofilin-actin rods. J Biol Chem *285*, 5450-5460. 10.1074/jbc.M109.063768.

40.   Bernstein, B.W., Chen, H., Boyle, J.A., and Bamburg, J.R. (2006). Formation of actin-ADF/cofilin rods transiently retards decline of mitochondrial potential and ATP

in stressed neurons. Am J Physiol Cell Physiol *291*, C828-839. 10.1152/ajpcell.00066.2006.

41.   Kelpsch, D.J., Groen, C.M., Fagan, T.N., Sudhir, S., and Tootle, T.L. (2016). Fascin regulates nuclear actin during Drosophila oogenesis. Mol Biol Cell *27*, 2965-2979. 10.1091/mbc.E15-09-0634.

42.   Ono, S., Abe, H., Nagaoka, R., and Obinata, T. (1993). Colocalization of ADF and cofilin in intranuclear actin rods of cultured muscle cells. J Muscle Res Cell Motil *14*, 195-204. 10.1007/BF00115454.

43.   Sanger, J.W., Sanger, J.M., Kreis, T.E., and Jockusch, B.M. (1980). Reversible translocation of cytoplasmic actin into the nucleus caused by dimethyl sulfoxide. Proc Natl Acad Sci U S A *77*, 5268-5272. 10.1073/pnas.77.9.5268.

44.   Vandebrouck, A., Domazetovska, A., Mokbel, N., Cooper, S.T., Ilkovski, B., and North, K.N. (2010). In vitro analysis of rod composition and actin dynamics in inherited myopathies. J Neuropathol Exp Neurol *69*, 429-441. 10.1097/NEN.0b013e3181d892c6.

45.   Munsie, L.N., Desmond, C.R., and Truant, R. (2012). Cofilin nuclear-cytoplasmic shuttling affects cofilin-actin rod formation during stress. J Cell Sci *125*, 3977-3988. 10.1242/jcs.097667.

46.   Cichon, J., Sun, C., Chen, B., Jiang, M., Chen, X.A., Sun, Y., Wang, Y., and Chen, G. (2012). Cofilin aggregation blocks intracellular trafficking and induces synaptic loss in hippocampal neurons. J Biol Chem *287*, 3919-3929. 10.1074/jbc.M111.301911.

47. Jang, D.H., Han, J.H., Lee, S.H., Lee, Y.S., Park, H., Lee, S.H., Kim, H., and Kaang, B.K. (2005). Cofilin expression induces cofilin-actin rod formation and disrupts synaptic structure and function in Aplysia synapses. Proc Natl Acad Sci U S A *102*, 16072-16077. 10.1073/pnas.0507675102.

48. Uruk, G., Mocanu, E., Shaw, A.E., Bamburg, J.R., and Swanson, R.A. (2024). Cofilactin rod formation mediates inflammation-induced neurite degeneration. Cell Rep *43*, 113914. 10.1016/j.celrep.2024.113914.

49. Almarghalani, D.A., Bahader, G.A., Ali, M., Tillekeratne, L.M.V., and Shah, Z.A. (2024). Cofilin Inhibitor Improves Neurological and Cognitive Functions after Intracerebral Hemorrhage by Suppressing Endoplasmic Reticulum Stress Related-Neuroinflammation. Pharmaceuticals (Basel) *17*. 10.3390/ph17010114.

50. Alhadidi, Q., Nash, K.M., Alaqel, S., Sayeed, M.S.B., and Shah, Z.A. (2018). Cofilin Knockdown Attenuates Hemorrhagic Brain Injury-induced Oxidative Stress and Microglial Activation in Mice. Neuroscience *383*, 33-45. 10.1016/j.neuroscience.2018.04.036.

51. Bahader, G.A., James, A.W., Almarghalani, D.A., and Shah, Z.A. (2023). Cofilin Inhibitor Protects against Traumatic Brain Injury-Induced Oxidative Stress and Neuroinflammation. Biology (Basel) *12*. 10.3390/biology12040630.

52. Lin, S., Wang, J., Cao, B., Huang, Y., Sheng, X., and Zhu, Y. (2023). Cofilin-1 induces acute kidney injury via the promotion of endoplasmic reticulum stress-mediated ferroptosis. Hum Cell *36*, 1928-1937. 10.1007/s13577-023-00949-9.

53. Posadas, I., Perez-Martinez, F.C., Guerra, J., Sanchez-Verdu, P., and Cena, V. (2012). Cofilin activation mediates Bax translocation to mitochondria during

excitotoxic neuronal death. J Neurochem *120*, 515-527. 10.1111/j.1471-4159.2011.07599.x.

54. Shu, L., Chen, B., Chen, B., Xu, H., Wang, G., Huang, Y., Zhao, Y., Gong, H., Jiang, M., Chen, L., et al. (2019). Brain ischemic insult induces cofilin rod formation leading to synaptic dysfunction in neurons. J Cereb Blood Flow Metab *39*, 2181-2195. 10.1177/0271678X18785567.

55. Chen, L., Cai, J., Huang, Y., Tan, X., Guo, Q., Lin, X., Zhu, C., Zeng, X., Liu, H., and Wu, X. (2020). Identification of cofilin-1 as a novel mediator for the metastatic potentials and chemoresistance of the prostate cancer cells. Eur J Pharmacol *880*, 173100. 10.1016/j.ejphar.2020.173100.

56. Kotiadis, V.N., Leadsham, J.E., Bastow, E.L., Gheeraert, A., Whybrew, J.M., Bard, M., Lappalainen, P., and Gourlay, C.W. (2012). Identification of new surfaces of cofilin that link mitochondrial function to the control of multi-drug resistance. J Cell Sci *125*, 2288-2299. 10.1242/jcs.099390.

57. Sousa-Squiavinato, A.C.M., and Morgado-Diaz, J.A. (2024). A glimpse into cofilin-1 role in cancer therapy: A potential target to improve clinical outcomes? Biochim Biophys Acta Rev Cancer *1879*, 189087. 10.1016/j.bbcan.2024.189087.

58. Alaqel, S.I., Dlamini, S., Almarghalani, D.A., Shettigar, A., Alhadidi, Q., Kodithuwakku, S.H., Stary, C., Tillekeratne, L.M.V., and Shah, Z.A. (2022). Synthesis and Development of a Novel First-in-Class Cofilin Inhibitor for Neuroinflammation in Hemorrhagic Brain Injury. ACS Chem Neurosci *13*, 1014-1029. 10.1021/acschemneuro.2c00010.

59. Shaw, A.E., and Bamburg, J.R. (2017). Peptide regulation of cofilin activity in the CNS: A novel therapeutic approach for treatment of multiple neurological disorders. Pharmacol Ther *175*, 17-27. 10.1016/j.pharmthera.2017.02.031.

60. Baum, B., and Perrimon, N. (2001). Spatial control of the actin cytoskeleton in Drosophila epithelial cells. Nat Cell Biol *3*, 883-890. 10.1038/ncb1001-883.

61. Blair, A., Tomlinson, A., Pham, H., Gunsalus, K.C., Goldberg, M.L., and Laski, F.A. (2006). Twinstar, the Drosophila homolog of cofilin/ADF, is required for planar cell polarity patterning. Development *133*, 1789-1797. 10.1242/dev.02320.

62. Chen, J., Godt, D., Gunsalus, K., Kiss, I., Goldberg, M., and Laski, F.A. (2001). Cofilin/ADF is required for cell motility during Drosophila ovary development and oogenesis. Nat Cell Biol *3*, 204-209. 10.1038/35055120.

63. Gunsalus, K.C., Bonaccorsi, S., Williams, E., Verni, F., Gatti, M., and Goldberg, M.L. (1995). Mutations in twinstar, a Drosophila gene encoding a cofilin/ADF homologue, result in defects in centrosome migration and cytokinesis. J Cell Biol *131*, 1243-1259. 10.1083/jcb.131.5.1243.

64. Zheng, L., Sepulveda, L.A., Lua, R.C., Lichtarge, O., Golding, I., and Sokac, A.M. (2013). The maternal-to-zygotic transition targets actin to promote robustness during morphogenesis. PLoS Genet *9*, e1003901. 10.1371/journal.pgen.1003901.

65. Bergh, S., and Arking, R. (1984). Development profile of the heat shock response in early embryos of Drosophila. J Exp Zool *231*, 379-391. 10.1002/jez.1402310312.

66. Orkenby, L., Skog, S., Ekman, H., Gozzo, A., Kugelberg, U., Ramesh, R., Magadi, S., Zambanini, G., Nordin, A., Cantu, C., et al. (2023). Stress-sensitive dynamics

of miRNAs and Elba1 in Drosophila embryogenesis. Mol Syst Biol *19*, e11148. 10.15252/msb.202211148.

67.   Wang, Z., and Lindquist, S. (1998). Developmentally regulated nuclear transport of transcription factors in Drosophila embryos enable the heat shock response. Development *125*, 4841-4850. 10.1242/dev.125.23.4841.

68.   Welte, M.A., Tetrault, J.M., Dellavalle, R.P., and Lindquist, S.L. (1993). A new method for manipulating transgenes: engineering heat tolerance in a complex, multicellular organism. Curr Biol *3*, 842-853. 10.1016/0960-9822(93)90218-d.

69.   Ashburner, M., Golic, K.G., and Hawley, R.S. (2005). Drosophila : a laboratory handbook, 2nd Edition (Cold Spring Harbor Laboratory Press).

70.   Crapse, J., Pappireddi, N., Gupta, M., Shvartsman, S.Y., Wieschaus, E., and Wuhr, M. (2021). Evaluating the Arrhenius equation for developmental processes. Mol Syst Biol *17*, e9895. 10.15252/msb.20209895.

71.   Gibbs, J.R., Mei, C., and Wunderlich, Z. (2024). Beyond the heat shock pathway: Heat stress responses in Drosophila development. Dev Biol *518*, 53-60. 10.1016/j.ydbio.2024.11.003.

72.   Kale, G., Agarwal, P., Diaz-Larrosa, J.J., and Lemke, S. (2024). Elevated temperature fatally disrupts nuclear divisions in the early Drosophila embryo. bioRxiv, 2023.2009.2017.558127. 10.1101/2023.09.17.558127.

73.   Kuntz, S.G., and Eisen, M.B. (2014). Drosophila embryogenesis scales uniformly across temperature in developmentally diverse species. PLoS Genet *10*, e1004293. 10.1371/journal.pgen.1004293.

74. Sokac, A.M., Biel, N., and De Renzis, S. (2023). Membrane-actin interactions in morphogenesis: Lessons learned from Drosophila cellularization. Semin Cell Dev Biol *133*, 107-122. 10.1016/j.semcdb.2022.03.028.

75. Grosshans, J., Wenzl, C., Herz, H.M., Bartoszewski, S., Schnorrer, F., Vogt, N., Schwarz, H., and Muller, H.A. (2005). RhoGEF2 and the formin Dia control the formation of the furrow canal by directed actin assembly during Drosophila cellularisation. Development *132*, 1009-1020. 10.1242/dev.01669.

76. Padash Barmchi, M., Rogers, S., and Hacker, U. (2005). DRhoGEF2 regulates actin organization and contractility in the Drosophila blastoderm embryo. J Cell Biol *168*, 575-585. 10.1083/jcb.200407124.

77. Sokac, A.M., and Wieschaus, E. (2008). Zygotically controlled F-actin establishes cortical compartments to stabilize furrows during Drosophila cellularization. J Cell Sci *121*, 1815-1824. 10.1242/jcs.025171.

78. Cao, J., Albertson, R., Riggs, B., Field, C.M., and Sullivan, W. (2008). Nuf, a Rab11 effector, maintains cytokinetic furrow integrity by promoting local actin polymerization. J Cell Biol *182*, 301-313. 10.1083/jcb.200712036.

79. Xue, Z., and Sokac, A.M. (2016). -Back-to-back mechanisms drive actomyosin ring closure during Drosophila embryo cleavage. J Cell Biol *215*, 335-344. 10.1083/jcb.201608025.

80. Mukhina, S., Wang, Y.L., and Murata-Hori, M. (2007). Alpha-actinin is required for tightly regulated remodeling of the actin cortical network during cytokinesis. Dev Cell *13*, 554-565. 10.1016/j.devcel.2007.08.003.

81. Biel, N., Figard, L., and Sokac, A.M. (2020). Imaging Intranuclear Actin Rods in Live Heat Stressed Drosophila Embryos. J Vis Exp. 10.3791/61297.

82. Knapp, B.D., and Huang, K.C. (2022). The Effects of Temperature on Cellular Physiology. Annu Rev Biophys *51*, 499-526. 10.1146/annurev-biophys-112221-074832.

83. Bownes, M. (1975). A photographic study of development in the living embryo of Drosophila melanogaster. J Embryol Exp Morphol *33*, 789-801.

84. Tadros, W., and Lipshitz, H.D. (2009). The maternal-to-zygotic transition: a play in two acts. Development *136*, 3033-3042. 10.1242/dev.033183.

85. Hu, Y., Comjean, A., Attrill, H., Antonazzo, G., Thurmond, J., Chen, W., Li, F., Chao, T., Mohr, S.E., Brown, N.H., and Perrimon, N. (2023). PANGEA: a new gene set enrichment tool for Drosophila and common research organisms. Nucleic Acids Res *51*, W419-W426. 10.1093/nar/gkad331.

86. Dicks, N., Bohrer, R.C., Gutierrez, K., Michalak, M., Agellon, L.B., and Bordignon, V. (2017). Relief of endoplasmic reticulum stress enhances DNA damage repair and improves development of pre-implantation embryos. PLoS One *12*, e0187717. 10.1371/journal.pone.0187717.

87. Michalak, M., and Gye, M.C. (2015). Endoplasmic reticulum stress in periimplantation embryos. Clin Exp Reprod Med *42*, 1-7. 10.5653/cerm.2015.42.1.1.

88. Blythe, S.A., and Wieschaus, E.F. (2016). Establishment and maintenance of heritable chromatin structure during early Drosophila embryogenesis. Elife *5*. 10.7554/eLife.20148.

89. Ko, C.S., Kalakuntla, P., and Martin, A.C. (2020). Apical Constriction Reversal upon Mitotic Entry Underlies Different Morphogenetic Outcomes of Cell Division. Mol Biol Cell *31*, 1663-1674. 10.1091/mbc.E19-12-0673.

90. Ray, M., Conard, A.M., Urban, J., Mahableshwarkar, P., Aguilera, J., Huang, A., Vaidyanathan, S., and Larschan, E. (2023). Sex-specific splicing occurs genome-wide during early Drosophila embryogenesis. Elife *12*. 10.7554/eLife.87865.

91. Riemondy, K., Henriksen, J.C., and Rissland, O.S. (2023). Intron dynamics reveal principles of gene regulation during the maternal-to-zygotic transition. RNA *29*, 596-608. 10.1261/rna.079168.122.

92. Chipman, A.D. (2020). The evolution of the gene regulatory networks patterning the Drosophila Blastoderm. Curr Top Dev Biol *139*, 297-324. 10.1016/bs.ctdb.2020.02.004.

93. Nusslein-Volhard, C., Kluding, H., and Jurgens, G. (1985). Genes affecting the segmental subdivision of the Drosophila embryo. Cold Spring Harb Symp Quant Biol *50*, 145-154. 10.1101/sqb.1985.050.01.020.

94. Martinez Arias, A., Baker, N.E., and Ingham, P.W. (1988). Role of segment polarity genes in the definition and maintenance of cell states in the Drosophila embryo. Development *103*, 157-170. 10.1242/dev.103.1.157.

95. Heer, N.C., and Martin, A.C. (2017). Tension, contraction and tissue morphogenesis. Development *144*, 4249-4260. 10.1242/dev.151282.

96. Leptin, M. (1991). twist and snail as positive and negative regulators during Drosophila mesoderm development. Genes Dev *5*, 1568-1576. 10.1101/gad.5.9.1568.

97. Perry, M.W., Boettiger, A.N., Bothma, J.P., and Levine, M. (2010). Shadow enhancers foster robustness of Drosophila gastrulation. Curr Biol *20*, 1562-1567. 10.1016/j.cub.2010.07.043.

98. Seong, K.H., Li, D., Shimizu, H., Nakamura, R., and Ishii, S. (2011). Inheritance of stress-induced, ATF-2-dependent epigenetic change. Cell *145*, 1049-1061. 10.1016/j.cell.2011.05.029.

99. Wang, L., Zeng, X., Ryoo, H.D., and Jasper, H. (2014). Integration of UPRER and oxidative stress signaling in the control of intestinal stem cell proliferation. PLoS Genet *10*, e1004568. 10.1371/journal.pgen.1004568.

100. Hetz, C., Zhang, K., and Kaufman, R.J. (2020). Mechanisms, regulation and functions of the unfolded protein response. Nat Rev Mol Cell Biol *21*, 421-438. 10.1038/s41580-020-0250-z.

101. Ron, D. (2002). Translational control in the endoplasmic reticulum stress response. J Clin Invest *110*, 1383-1388. 10.1172/JCI16784.

102. Bhattarai, K.R., Riaz, T.A., Kim, H.R., and Chae, H.J. (2021). The aftermath of the interplay between the endoplasmic reticulum stress response and redox signaling. Exp Mol Med *53*, 151-167. 10.1038/s12276-021-00560-8.

103. Khatun, H., Ihara, Y., Takakura, K., Egashira, J., Wada, Y., Konno, T., Tatemoto, H., and Yamanaka, K.I. (2020). Role of endoplasmic reticulum stress on developmental competency and cryo-tolerance in bovine embryos. Theriogenology *142*, 131-137. 10.1016/j.theriogenology.2019.09.042.

104. Dutta, N., Garcia, G., and Higuchi-Sanabria, R. (2022). Hijacking Cellular Stress Responses to Promote Lifespan. Front Aging *3*, 860404. 10.3389/fragi.2022.860404.

105. Houtkooper, R.H., Mouchiroud, L., Ryu, D., Moullan, N., Katsyuba, E., Knott, G., Williams, R.W., and Auwerx, J. (2013). Mitonuclear protein imbalance as a conserved longevity mechanism. Nature *497*, 451-457. 10.1038/nature12188.

106. Labbadia, J., Brielmann, R.M., Neto, M.F., Lin, Y.F., Haynes, C.M., and Morimoto, R.I. (2017). Mitochondrial Stress Restores the Heat Shock Response and Prevents Proteostasis Collapse during Aging. Cell Rep *21*, 1481-1494. 10.1016/j.celrep.2017.10.038.

107. Lockwood, B.L., Julick, C.R., and Montooth, K.L. (2017). Maternal loading of a small heat shock protein increases embryo thermal tolerance in Drosophila melanogaster. J Exp Biol *220*, 4492-4501. 10.1242/jeb.164848.

108. Pribenszky, C., Losonczi, E., Molnar, M., Lang, Z., Matyas, S., Rajczy, K., Molnar, K., Kovacs, P., Nagy, P., Conceicao, J., and Vajta, G. (2010). Prediction of in-vitro developmental competence of early cleavage-stage mouse embryos with compact time-lapse equipment. Reprod Biomed Online *20*, 371-379. 10.1016/j.rbmo.2009.12.007.

109. Quiros, P.M., Mottis, A., and Auwerx, J. (2016). Mitonuclear communication in homeostasis and stress. Nat Rev Mol Cell Biol *17*, 213-226. 10.1038/nrm.2016.23.

110. Yun, J., and Finkel, T. (2014). Mitohormesis. Cell Metab *19*, 757-766. 10.1016/j.cmet.2014.01.011.

111. Christians, E.S. (2017). Heat Shock Proteins and Maternal Contribution to Oogenesis and Early Embryogenesis. In The Role of Heat Shock Proteins in Reproductive System Development and Function, D.J. MacPhee, ed. (Springer International Publishing), pp. 1-27. 10.1007/978-3-319-51409-3_1.

112. Feder, M.E., Cartano, N.V., Milos, L., Krebs, R.A., and Lindquist, S.L. (1996). Effect of engineering Hsp70 copy number on Hsp70 expression and tolerance of ecologically relevant heat shock in larvae and pupae of Drosophila melanogaster. J Exp Biol *199*, 1837-1844. 10.1242/jeb.199.8.1837.

113. Roberts, S.P., and Feder, M.E. (1999). Natural hyperthermia and expression of the heat shock protein Hsp70 affect developmental abnormalities in Drosophila melanogaster. Oecologia *121*, 323-329. 10.1007/s004420050935.

114. Rutherford, S.L., and Lindquist, S. (1998). Hsp90 as a capacitor for morphological evolution. Nature *396*, 336-342. 10.1038/24550.

115. Sangster, T.A., Lindquist, S., and Queitsch, C. (2004). Under cover: causes, effects and implications of Hsp90-mediated genetic capacitance. Bioessays *26*, 348-362. 10.1002/bies.20020.

116. Graziosi, G., Micali, F., Marzari, R., de Cristini, F., and Savoini, A. (1980). Variability of response of early Drosophila embryos to heat shock. Journal of Experimental Zoology *214*, 141-145. 10.1002/jez.1402140203.

117. Luo, S., Uehara, H., and Shacter, E. (2014). Taurine chloramine-induced inactivation of cofilin protein through methionine oxidation. Free Radic Biol Med *75*, 84-94. 10.1016/j.freeradbiomed.2014.07.018.

118. Copeland, J.M., Cho, J., Lo, T., Jr., Hur, J.H., Bahadorani, S., Arabyan, T., Rabie, J., Soh, J., and Walker, D.W. (2009). Extension of Drosophila life span by RNAi of the mitochondrial respiratory chain. Curr Biol *19*, 1591-1598. 10.1016/j.cub.2009.08.016.

119. Dillin, A., Hsu, A.L., Arantes-Oliveira, N., Lehrer-Graiwer, J., Hsin, H., Fraser, A.G., Kamath, R.S., Ahringer, J., and Kenyon, C. (2002). Rates of behavior and aging specified by mitochondrial function during development. Science *298*, 2398-2401. 10.1126/science.1077780.

120. Owusu-Ansah, E., Song, W., and Perrimon, N. (2013). Muscle mitohormesis promotes longevity via systemic repression of insulin signaling. Cell *155*, 699-712. 10.1016/j.cell.2013.09.021.

121. Fang, X., Chen, T., Tran, K., and Parker, C.S. (2001). Developmental regulation of the heat shock response by nuclear transport factor karyopherin-alpha3. Development *128*, 3349-3358. 10.1242/dev.128.17.3349.

122. Xu, H., Sepulveda, L.A., Figard, L., Sokac, A.M., and Golding, I. (2015). Combining protein and mRNA quantification to decipher transcriptional regulation. Nat Methods *12*, 739-742. 10.1038/nmeth.3446.

123. Dobin, A., Davis, C.A., Schlesinger, F., Drenkow, J., Zaleski, C., Jha, S., Batut, P., Chaisson, M., and Gingeras, T.R. (2013). STAR: ultrafast universal RNA-seq aligner. Bioinformatics *29*, 15-21. 10.1093/bioinformatics/bts635.

124. Anders, S., Pyl, P.T., and Huber, W. (2015). HTSeq--a Python framework to work with high-throughput sequencing data. Bioinformatics *31*, 166-169. 10.1093/bioinformatics/btu638.

125. Robinson, M.D., McCarthy, D.J., and Smyth, G.K. (2010). edgeR: a Bioconductor package for differential expression analysis of digital gene expression data. Bioinformatics *26*, 139-140. 10.1093/bioinformatics/btp616.

126. Livak, K.J., and Schmittgen, T.D. (2001). Analysis of relative gene expression data using real-time quantitative PCR and the 2(-Delta Delta C(T)) Method. Methods *25*, 402-408. 10.1006/meth.2001.1262.

127. Schmittgen, T.D., and Livak, K.J. (2008). Analyzing real-time PCR data by the comparative C(T) method. Nat Protoc *3*, 1101-1108. 10.1038/nprot.2008.73.

128. Perez-Riverol, Y., Bai, J., Bandla, C., Garcia-Seisdedos, D., Hewapathirana, S., Kamatchinathan, S., Kundu, D.J., Prakash, A., Frericks-Zipper, A., Eisenacher, M., et al. (2022). The PRIDE database resources in 2022: a hub for mass spectrometry-based proteomics evidences. Nucleic Acids Res *50*, D543-D552. 10.1093/nar/gkab1038.

A

Egg deposition — Embryos collected for experiments

18°C / 32°C

18°C
Acute 1.5 hr, 32°C
Chronic 12 hr, 32°C

Syncytial development | Cellularization

B

18°C   Acute 32°C   Chronic 32°C
***   ***   ***

Live larvae (%)

WT   cofilin+/-   WT   cofilin+/-   WT   cofilin+/-

C

18°C   Acute 32°C   Chronic 32°C
***   ***   ***

Live adults (%)

WT   cofilin+/-   WT   cofilin+/-   WT   cofilin+/-

D

WT
18°C   Acute 32°C   Chronic 32°C
Pre
Bleach
20 s
50 s
Actin

cofilin+/-
18°C   Acute 32°C   Chronic 32°C
Pre
Bleach
20 s
50 s
Actin

E

n.s.
*
*
***
***
***

Half-time (s)

WT: 18°C   Acute 32°C   Chronic 32°C
cofilin+/-: 18°C   Acute 32°C   Chronic 32°C

F

WT
18°C   Acute 32°C   Chronic 32°C

cofilin+/-
18°C   Acute 32°C   Chronic 32°C
Actin

G

*
***
***

Embryos with rods (%)

WT: 18°C   Acute 32°C   Chronic 32°C
cofilin+/-: 18°C   Acute 32°C   Chronic 32°C

H

***
n.s.
***
***
***

Rods/nucleus

WT: 18°C   Acute 32°C   Chronic 32°C
cofilin+/-: 18°C   Acute 32°C   Chronic 32°C

A WT acute 32°C

B WT chronic 32°C

C

Foci | Color | *twist* expression

2 foci / 1 foci → "ON"

0 foci → "OFF"

18°C

Chronic 32°C

ventral tissue

Segmented

Nuclei *twist*

D

Number of nuclei with *twist* expression

18°C   Chronic 32°C

E

Nuclei per embryo (%)

18°C: 2 foci, 1 foci, 0 foci   Chronic 32°C: 2 foci, 1 foci, 0 foci

A Acute 32°C

B Chronic 32°C

C cofilin⁺/⁻ 18°C

D cofilin⁺/⁻ 18°C
Mitochondrial translation/respiration genes

E cofilin⁺/⁻ 18°C
Heat stress genes

F cofilin⁺/⁻ 18°C
Cytoplasmic translation genes

G cofilin⁺/⁻ 18°C
ER stress genes

H cofilin⁺/⁻ 18°C
Segmentation genes